
Learning perturbation sets for robust machine learning

Eric Wong

Machine Learning Department
Carnegie Mellon University
Pittsburgh, PA 15213
ericwong@cs.cmu.edu

J. Zico Kolter

Computer Science Department
Carnegie Mellon University
Pittsburgh, PA 15213
zkolter@cs.cmu.edu

Abstract

Although much progress has been made towards robust deep learning, a significant gap in robustness remains between real-world perturbations and more narrowly defined sets typically studied in adversarial defenses. In this paper, we aim to bridge this gap by *learning* perturbation sets from data, in order to characterize real-world effects for robust training and evaluation. Specifically, we use a conditional generator that defines the perturbation set over a constrained region of the latent space. We formulate desirable properties that measure the quality of a learned perturbation set, and theoretically prove that a conditional variational autoencoder naturally satisfies these criteria. Using this framework, our approach can generate a variety of perturbations at different complexities and scales, ranging from baseline digit transformations, through common image corruptions, to lighting variations. We measure the quality of our learned perturbation sets both quantitatively and qualitatively, finding that our models are capable of producing a diverse set of meaningful perturbations beyond the limited data seen during training. Finally, we leverage our learned perturbation sets to learn models which have improved generalization performance and are empirically and certifiably robust to adversarial image corruptions and adversarial lighting variations. All code and configuration files for reproducing the experiments as well as pretrained model weights can be found at https://github.com/locuslab/perturbation_learning.

1 Introduction

Within the last decade, adversarial learning has become a core research area for studying robustness and machine learning. Adversarial attacks have expanded well beyond the original setting of imperceptible noise to more general notions of robustness, and can broadly be described as capturing sets of perturbations that humans are naturally invariant to. These invariants form the motivation of many real world adversarial attacks, for example facial recognition should be robust to adversarial glasses [Sharif et al., 2019] or traffic sign classification should be robust to adversarial graffiti [Eykholt et al., 2018]. However, human invariants can also include notions which are not inherently adversarial, for example image classifiers should be robust to common image corruptions [Hendrycks and Dietterich, 2019] as well as changes in weather patterns [Michaelis et al., 2019].

On the other hand, although there has been much success in defending against small adversarial perturbations, most successful and principled methods for learning robust models are limited to human invariants that can be characterized using mathematically defined perturbation sets, for example perturbations bounded in ℓ_p norm. After all, established guidelines for evaluating adversarial robustness [Carlini et al., 2019] have emphasized the importance of the perturbation set (or the threat model) as a necessary component for performing proper, scientific evaluations of adversarial defense

proposals. However, this requirement makes it difficult to learn models which are robust to human invariants beyond these mathematical sets, where real world attacks and general notions of robustness can often be virtually impossible to write down as a formal set of equations. This incompatibility between existing methods for learning robust models and real-world, human invariants raises a fundamental question for the field of robust machine learning:

How can we learn models that are robust to perturbations without a mathematical definition?

In the absence of a mathematical definition, in this work we present a general framework for learning perturbation sets from perturbed data. More concretely, given pairs of examples where one is a perturbed version of the other, we propose learning generative models that can “perturb” an example by varying a fixed region of the underlying latent space. The resulting perturbation sets are well-defined and can easily be used in robust training and evaluation tasks. The approach is widely applicable to a range of robustness settings, as we make no assumptions on the type of perturbation being learned: the only requirement is to collect examples of perturbed data.

Given the susceptibility of deep learning to adversarial examples, such a perturbation set will undoubtedly come under intense scrutiny, especially if it is to be used as a threat model for adversarial attacks. In this paper, we begin with a broad discussion of perturbation sets and formulate deterministic and probabilistic properties that a learned perturbation set should have in order to be a meaningful proxy for the true underlying perturbation set. The *necessary subset* property ensures that the set captures real perturbations, properly motivating its usage as an adversarial threat model. The *sufficient likelihood* property ensures that real perturbations have high probability, which motivates sampling from a perturbation set as a form of data augmentation. We then prove the main theoretical result, that a learned perturbation set defined by the decoder and prior of a conditional variational autoencoder (CVAE) [Sohn et al., 2015] implies both of these properties, providing a theoretically motivated framework for learning perturbation sets. The quality of a CVAE can be further evaluated with metrics from probabilistic generative modeling such as the likelihood lower bound and samples drawn from the prior. The resulting CVAE perturbation sets are well motivated, can leverage standard architectures, and are computationally efficient with little tuning required.

We highlight the versatility of our approach using CVAEs with an array of experiments, where we vary the complexity and scale of the datasets, perturbations, and downstream tasks. We first demonstrate how the approach can learn basic ℓ_∞ and rotation-translation-skew (RTS) perturbations [Jaderberg et al., 2015] in the MNIST setting. Since these sets can be mathematically defined, our goal is simply to measure exactly how well the learned perturbation set captures the target perturbation set on baseline tasks where the ground truth is known. We next look at a more difficult setting which can not be mathematically defined, and learn a perturbation set for common image corruptions on CIFAR10 [Hendrycks and Dietterich, 2019]. The resulting perturbation set can interpolate between common corruptions, produce diverse samples, and be used in adversarial training and randomized smoothing frameworks. The adversarially trained models have improved generalization performance to both in- and out-of-distribution corruptions and better robustness to adversarial corruptions. In our final setting, we learn a perturbation set that captures variations in lighting using a multi-illumination dataset of scenes captured “in the wild” [Murrman et al., 2019]. The perturbation set generates meaningful lighting samples and interpolations while generalizing to unseen scenes, and can be used to learn image segmentation models that are empirically and certifiably robust to lighting changes. All code and configuration files for reproducing the experiments as well as pretrained model weights for both the learned perturbation sets as well as the downstream robust classifiers can be found at https://github.com/locuslab/perturbation_learning.

2 Background and related work

Perturbation sets for adversarial threat models Adversarial examples were initially defined as imperceptible examples with small ℓ_1 , ℓ_2 and ℓ_∞ norm [Biggio et al., 2013, Szegedy et al., 2013, Goodfellow et al., 2014], forming the earliest known, well-defined perturbation sets that were eventually generalized to the union of multiple ℓ_p perturbations [Tramèr and Boneh, 2019, Maini et al., 2019, Croce and Hein, 2019, Stutz et al., 2019]. Alternative perturbation sets to the ℓ_p setting that remain well-defined incorporate more structure and semantic meaning, such as rotations and translations [Engstrom et al., 2017], Wasserstein balls [Wong et al., 2019], functional perturbations

[Laidlaw and Feizi, 2019], distributional shifts [Sinha et al., 2017, Sagawa et al., 2019], word embeddings [Miyato et al., 2016], and word substitutions [Alzantot et al., 2018, Jia et al., 2019].

Other work has studied perturbation sets that are not necessarily mathematically formulated but well-defined from a human perspective such as spatial transformations [Xiao et al., 2018b]. Real-world adversarial attacks tend to try to remain either inconspicuous to the viewer or meddle with features that humans would naturally ignore, such as textures on 3D printed objects [Athalye et al., 2017], graffiti on traffic signs [Eykholt et al., 2018], shapes of objects to avoid LiDAR detection [Cao et al., 2019], irrelevant background noise for audio [Li et al., 2019a], or barely noticeable films on cameras [Li et al., 2019b]. Although not necessarily adversarial, Hendrycks and Dietterich [2019] propose the set of common image corruptions as a measure of robustness to informal shifts in distribution.

Generative modeling and adversarial robustness Relevant to our work is that which combines aspects of generative modeling with adversarial examples [Xiao et al., 2018a, Song et al., 2018, Sharif et al., 2019, Bhattad et al., 2020], most of which either use ℓ_p perturbations, run user studies to define the perturbation set, or simply do not restrict the adversary at all. Goyal et al. [2019] trained a StyleGAN to disentangle real-world perturbations when no perturbation information is known in advance. However the resulting perturbation set relies on a stochastic approximation, and it is not immediately obvious what this set will ultimately capture. Perhaps most similar is the concurrent work of Robey et al. [2020], which uses a GAN architecture for image-to-image translation to model simple perturbations. In contrast to both of these works, our setting is more targeted and leverages the observation that pairs of inputs come from the same perturbation set, directly learning *how* to perturb from perturbed pairs of examples without needing to disentangle any features or learn how to translate entire datasets. Furthermore, we formulate desirable properties of perturbation sets for downstream robustness tasks, and formally prove that a conditional variational autoencoder approach satisfies these properties. This results in a principled framework for learning perturbation sets that is quite distinct from the GAN-based approaches in both setting and motivation.

Adversarial defenses and data augmentation Successful approaches for learning adversarially robust networks include methods which are both empirically robust via adversarial training [Goodfellow et al., 2014, Kurakin et al., 2016, Madry et al., 2017] and also certifiably robust via provable bounds [Wong and Kolter, 2017, Wong et al., 2018, Raghunathan et al., 2018, Goyal et al., 2018, Zhang et al., 2019] and randomized smoothing [Cohen et al., 2019, Yang et al., 2020]. Critically, these defenses require mathematically-defined perturbation sets, which has limited these approaches from learning robustness to more general, real-world perturbations. We directly build upon these approaches by learning perturbation sets that can be naturally incorporated into robust training, greatly expanding the scope of adversarial defenses to new contexts. Our work also relates to using non-adversarial perturbations via data augmentation to reduce generalization error [Zhang et al., 2017, DeVries and Taylor, 2017, Cubuk et al., 2019], which can occasionally also improve robustness to unrelated image corruptions [Geirhos et al., 2018, Hendrycks et al., 2019, Rusak et al., 2020]. Our work differs in that rather than aggregating or proposing generic data augmentations, our perturbation sets can provide data augmentation that is targeted for a particular robustness setting.

3 Perturbation sets learned from data

For an example $x \in \mathbb{R}^m$, a perturbation set $\mathcal{S}(x) \subseteq \mathbb{R}^m$ is defined informally as the set of examples which are considered to be equivalent to x , and hence can be viewed as “perturbations” of x . This set is often used when finding an adversarial example, which is typically cast as an optimization problem to maximize the loss of a model over the perturbation set in order to break the model. For example, for a classifier h , loss function ℓ , and label y , an adversarial attack tries to solve the following:

$$\underset{x' \in \mathcal{S}(x)}{\text{maximize}} \ell(h(x'), y). \quad (1)$$

A common choice for $\mathcal{S}(x)$ is an ℓ_p ball around the unperturbed example, defined as $\mathcal{S}(x) = \{x + \delta : \|\delta\|_p \leq \epsilon\}$ for some norm p and radius ϵ . This type of perturbation captures unstructured random noise, and is typically taken with respect to ℓ_p norms for $p \in \{0, 1, 2, \infty\}$, though more general distance metrics can also be used.

Although defining the perturbation set is critical for developing adversarial defenses, in some scenarios, the *true* perturbation set may be difficult to mathematically describe. In these settings, it may still

be possible to collect observations of (non-adversarial) perturbations, e.g. pairs of examples (x, \tilde{x}) where \tilde{x} is the *perturbed data*. In other words, \tilde{x} is a real, perturbed version of x , from which we can learn an approximation of the true perturbation set. While there are numerous possible approaches one can take to learn $\mathcal{S}(x)$ from examples (x, \tilde{x}) , in this work we take a generative modeling perspective, where examples are perturbed via an underlying latent space. Specifically, let $g : \mathbb{R}^k \times \mathbb{R}^m \rightarrow \mathbb{R}^m$ be a generator that takes a k -dimensional latent vector and an input, and outputs a perturbed version of the input. Then, we can define a *learned* perturbation set as follows:

$$\mathcal{S}(x) = \{g(z, x) : \|z\| \leq \epsilon\} \quad (2)$$

In other words, we have taken a well-defined perturbation set in the latent space (in this case, a norm-bounded ball) and mapped it to a set of perturbations with a generator g , which perturbs x into \tilde{x} via a latent code z . We can also define a perturbation set from a *probabilistic graphical modeling* perspective, and use a distribution over the latent space to parameterize a distribution over examples. Specifically, $\mathcal{S}(x)$ is now a random variable defined by a probability distribution $p_\epsilon(z)$ over the latent space as follows:

$$\mathcal{S}(x) \sim p_\theta \text{ such that } \theta = g(z, x), \quad z \sim p_\epsilon \quad (3)$$

where p_ϵ has support $\{z : \|z\| \leq \epsilon\}$ and p_θ is a distribution parameterized by $\theta = g(z, x)$.

3.1 General measures of quality for perturbation sets

A perturbation set defined by a generative model that is learned from data lacks the mathematical rigor of previous sets, so care must be taken to properly evaluate how well the model captures real perturbations. In this section we formally define two properties relating a perturbation set to data, which capture natural qualities of a perturbation set that are useful for adversarial robustness and data augmentation. We note that all quantities discussed in this paper can be calculated on both the training and testing sets, which allow us to concretely measure how well the perturbation set generalizes to unseen datapoints. For this section, let $d : \mathbb{R}^m \times \mathbb{R}^m \rightarrow \mathbb{R}$ be an distance metric (e.g. mean squared error) and let $x, \tilde{x} \in \mathbb{R}^m$ be a perturbed pair, where \tilde{x} is a perturbed version of x .

To be a reasonable threat model for adversarial examples, one desirable expectation is that a perturbation set should at least contain close approximations of the perturbed data. In other words, perturbed data should be (approximately) a *necessary subset* of the perturbation set. This notion of containment can be described more formally as follows:

Definition 1. A perturbation set $\mathcal{S}(x)$ satisfies the necessary subset property at approximation error at most δ for a perturbed pair (x, \tilde{x}) if there exists an $x' \in \mathcal{S}(x)$ such that $d(x', \tilde{x}) \leq \delta$.

For a perturbation set defined by the generative model from Equation (2), this amounts to finding a latent vector z which best approximates the perturbed example \tilde{x} by solving the following problem:

$$\min_{\|z\| \leq \epsilon} d(g(z, x), \tilde{x}). \quad (4)$$

This approximation error can be upper bounded by point estimates (e.g. by using an encoded representation of \tilde{x} projected onto the ϵ ball), or can be solved more accurately by using standard projected gradient descent. Note that mathematically-defined perturbation sets such as ℓ_p balls around clean datapoints naturally have zero approximation error (they contain all possible observations).

Our second desirable property is specific to the probabilistic setting from Equation (3), where we would expect perturbed data to have a high probability of occurring under a probabilistic perturbation set. In other words, a perturbation set should assign *sufficient likelihood* to perturbed data, described more formally in the following definition for our generative approach:

Definition 2. A probabilistic perturbation set $\mathcal{S}(x)$ satisfies the sufficient likelihood property at likelihood at least δ for a perturbed pair (x, \tilde{x}) if $\mathbb{E}_{p_\epsilon(z)}[p_\theta(\tilde{x})] \geq \delta$ where $\theta = g(z, x)$.

A model that assigns high likelihood to perturbed observations is likely to generate meaningful samples, which can then be used as a form of data augmentation in settings that care more about average-case over worst-case robustness. To measure this property, the likelihood can be approximated with a standard Monte Carlo estimate by sampling from the prior p_ϵ .

4 Variational autoencoders for learning perturbations sets

In this section we will focus on one possible approach using variational autoencoders (VAEs) to learn the perturbation set. Specifically, we will use the conditional variational autoencoder (CVAE) framework [Sohn et al., 2015], where we condition on the example being perturbed. We shift notation here to be consistent with the CVAE literature and consider a standard CVAE trained to predict $x \in \mathbb{R}^m$ from a latent space $z \in \mathbb{R}^k$ conditioned on some y , where in our context, x is a perturbed version of y . Let the posterior distribution $q(z|x, y)$, prior distribution $p(z|y)$, and likelihood function $p(x|z, y)$ be the following multivariate normal distributions with diagonal variance:

$$q(z|x, y) \sim \mathcal{N}(\mu(x, y), \sigma^2(x, y)), \quad p(z|y) \sim \mathcal{N}(\mu(y), \sigma^2(y)), \quad p(x|z, y) \sim \mathcal{N}(g(z, y), I) \quad (5)$$

where $\mu(x, y)$, $\sigma^2(x, y)$, $\mu(y)$, $\sigma^2(y)$, and $g(z, y)$ are arbitrary functions representing the respective encoder, prior, and decoder networks. CVAEs are trained by maximizing a likelihood lower bound

$$\log p(x|y) \geq \mathbb{E}_{q(z|x, y)}[\log p(x|z, y)] - KL(q(z|x, y)||p(z|y)) \quad (6)$$

also known as the SGVB estimator, where $KL(\cdot||\cdot)$ is the KL divergence. The CVAE framework lends to a natural and obvious (probabilistic) perturbation set by simply restricting the latent space to an ℓ_2 ball that is scaled and shifted by the prior network. For convenience, we will define the perturbation set in the latent space *before* the reparameterization trick, so the latent perturbation set for all examples is a standard ℓ_2 ball $\{u : \|u\|_2 \leq \epsilon\}$ where $z = u \cdot \sigma(y) + \mu(y)$. Similarly, a probabilistic perturbation set can be defined by simply truncating the prior distribution at radius ϵ (also before the reparameterization trick).

4.1 Theoretical connection from CVAEs to perturbation sets

Our theoretical results motivate why the CVAE is a reasonable framework for learning perturbation sets by proving that optimizing the CVAE objective results in both properties outlined in Section 3.1. Note that these results are not immediately obvious, since the likelihood of the CVAE objective is taken over the full posterior while the perturbation set is defined over a constrained latent subspace determined by the prior. The proofs rely heavily on the multivariate normal parameterizations, with several supporting results that bound various quantities relating the posterior and prior distributions. We give a concise, informal presentation of the main theoretical results in this section, deferring the full details, proofs, and supporting results to Appendix A. Our results are based on the minimal assumption that the CVAE objective has been trained to some thresholds as described in Assumption 1.

Assumption 1. *The CVAE objective has been trained to some thresholds R, K_i as follows*

$$\mathbb{E}_{q(z|x, y)}[\log p(x|z, y)] \geq R, \quad KL(q(z|x, y)||p(z|y)) \leq \frac{1}{2} \sum_{i=1}^k K_i$$

where each K_i bounds the KL-divergence of the i th dimension.

Our first theorem, Theorem 1, states that the approximation error of a perturbed example is bounded by the components of the CVAE objective. The implication here is that with enough representational capacity to optimize the objective, one can satisfy the necessary subset property by training a CVAE, effectively capturing perturbed data at low approximation error in the resulting perturbation set.

Theorem 1. *Let r be the Mahalanobis distance which captures $1 - \alpha$ of the probability mass for a k -dimensional standard multivariate normal for some $0 < \alpha < 1$. Then, there exists a z such that*

$$\left\| \frac{z - \mu(y)}{\sigma(y)} \right\|_2 \leq \epsilon \text{ and } \|g(z, y) - x\|_2 \leq \delta \text{ for}$$

$$\epsilon = Br + \sqrt{\sum_i K_i}, \quad \delta = -\frac{1}{1 - \alpha} (2R + m \log(2\pi))$$

where B is a constant dependent on K_i . Moreover, as $R \rightarrow -\frac{1}{2}m \log(2\pi)$ and $K_i \rightarrow 0$ (the theoretical limits of these bounds¹), then $\epsilon \rightarrow r$ and $\delta \rightarrow 0$.

¹In practice, VAE architectures in general have a non-trivial gap from the approximating posterior which make these theoretical limits unattainable.

Our second theorem, Theorem 2, states that the expected approximation error over the truncated prior can also be bounded by components of the CVAE objective. Since the generator g parameterizes a multivariate normal with identity covariance, an upper bound on the expected reconstruction error implies a lower bound on the likelihood. This implies that one can also satisfy the sufficient likelihood property by training a CVAE, effectively learning a probabilistic perturbation set that assigns high likelihood to perturbed data.

Theorem 2. *Let r be the Mahalanobis distance which captures $1 - \alpha$ of the probability mass for a k -dimensional standard multivariate normal for some $0 < \alpha < 1$. Then, the truncated expected approximation error can be bounded with*

$$\mathbb{E}_{p_r(u)} [\|g(u \cdot \sigma(y) + \mu(y), y) - x\|_2^2] \leq -\frac{1}{1 - \alpha} (2R + m \log(2\pi))H$$

where $p_r(u)$ is a multivariate normal that has been truncated to radius r and H is a constant that depends exponentially on K_i and r .

The main takeaway from these two theorems is that optimizing the CVAE objective naturally results in a learned perturbation set which satisfies the necessary subset and sufficient likelihood properties. The learned perturbation set is consequently useful for adversarial robustness since the necessary subset property implies that the perturbation set does not “miss” perturbed data. It is also useful for data augmentation since the sufficient likelihood property ensures that perturbed data occurs with high probability. We leave further discussion of these two theorems to Appendix A.3.

5 Experiments

Finally, we present a variety of experiments to showcase the generality and effectiveness of our perturbation sets learned with a CVAE. We note that our approach is broadly applicable, has no specific requirements for the encoder, decoder, and prior networks, and avoids the unstable training dynamics found in GANs. Additionally, since the CVAE is conditioned on an example, the CVAE can produce non-blurry images since it only needs to learn how to apply a perturbation and not reconstruct the entire image. All code, configuration files, and pretrained model weights for reproducing our experiments are included in the supplementary material and will be released with the paper.

In all settings, we train perturbation sets and evaluate them with a number of metrics averaged over the test set. To evaluate the necessary subset property, we provide two measures of the approximation error (AE): a cheap upper bound formed by projecting the mean of the posterior encoding onto the perturbation set (Enc. AE) and a refined upper bound using projected gradient descent (PGD AE). To evaluate the sufficient likelihood property, we calculate the expected approximation error (EAE) with a Monte Carlo estimate over five samples for each datapoint. To give a sense of how much a perturbation can diverge within the set, we calculate the overapproximation error (OAE) by maximizing the approximation error with projected gradient descent. Finally, we report CVAE metrics, the reconstruction error over the full posterior and the KL divergence. The final radius ϵ of the perturbation set is conservatively selected as the maximum ℓ_2 norm of the posterior mean unparameterized by the prior distribution, which is calculated over a held-out validation set. Further details and discussion for all these metrics and parameters can be found in Appendix B.

We highlight how our learned perturbation sets can be naturally leveraged in downstream robustness tasks by simply using existing techniques for ℓ_2 robustness directly on the latent space. For example, robust training and evaluation can be naturally done with a standard ℓ_2 PGD adversary [Madry et al., 2017] and a typical randomized smoothing defense [Cohen et al., 2019] can be done using Gaussian noise. Data augmentation can be performed by sampling from the truncated prior. We report standard performance on the original unperturbed dataset as “clean accuracy” and performance on perturbed data as “perturbed accuracy.” We also report accuracy under an ℓ_2 adversary as “robust accuracy” and certified performance under a standard ℓ_2 randomized smoothing procedure as “certified accuracy.” In the remainder of this section, we provide a summary of the main empirical results and leave additional details, visualizations, and supplementary experiments in Appendix C for MNIST, Appendix D for CIFAR10 common corruptions, and Appendix E for the multi-illumination dataset.

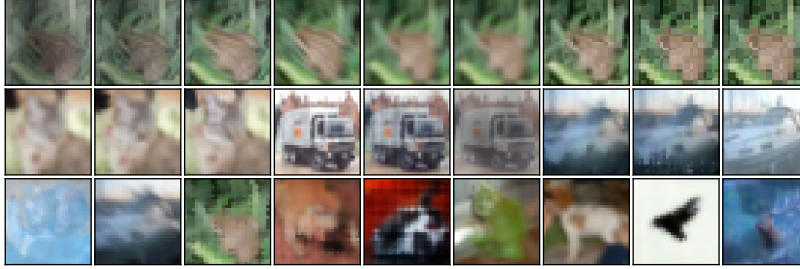


Figure 1: Visualization of a learned perturbation set trained on CIFAR10 common corruptions. (top row) Interpolations from fog, through defocus blur, to pixelate corruptions. (middle row) Random corruption samples for three examples. (bottom row) Adversarial corruptions that misclassify an adversarially trained classifier at $\epsilon = 10.2$.

Table 1: Adversarial robustness to CIFAR10 common corruptions with a CVAE perturbation set.

Method	Test set accuracy (%)			Test set robust accuracy (%)		
	Clean	Perturbed	OOD	$\epsilon = 2.7$	$\epsilon = 3.9$	$\epsilon = 10.2$
Data augmentation	90.6	87.7	85.0	42.4	37.2	17.8
CVAE data augmentation	94.5	90.5	89.6	68.6	63.3	43.4
CVAE adversarial training	94.6	90.3	89.9	72.1	66.1	55.6

5.1 MNIST perturbations

We briefly discuss some benchmark tasks on MNIST, where the perturbation set is mathematically-defined. Since an exact perturbation set will always be better than a learned approximation, the goal here is simply to measure the representational power of the CVAE for learning perturbations and establish a baseline where the ground truth is known. We consider learning the classic ℓ_∞ perturbation and rotation-translation-skew (RTS) perturbations [Jaderberg et al., 2015]. Specific perturbation, architecture, and training details are in Appendix C.1. Since an infinite amount of perturbed data can be generated, we report means and standard deviations calculated from five passes over the test set with randomly generated perturbations, and also train two additional models whose training set is limited to $N \in \{1, 5\}$ fixed perturbations per datapoint.

We show samples from the learned perturbation sets in Figure 4 of Appendix C.2, and perform a quantitative evaluation in Table 2 of Appendix C.3. Our first takeaway here is that RTS perturbations are much easier to learn than ℓ_∞ perturbations, but can be improved with convolutional architectures. We also find that a CVAE trained on data that is limited to just one perturbation per datapoint can achieve low approximation error on par with infinitely many perturbations per datapoint. Increasing this from one to five perturbations per datapoint can match all remaining metrics, which suggests that only a modest amount of perturbed data is needed to learn perturbation sets.

5.2 CIFAR10 common corruptions

In this section, we learn a perturbation set which captures common image corruptions for CIFAR10 which are considered to be out-of-distribution relative to the original CIFAR10 dataset [Hendrycks and Dietterich, 2019].² We focus on the highest severity level of the blur, weather, and digital categories, resulting in 12 different corruptions which capture more “natural” corruptions that are unlike random ℓ_p noise as described in Appendix D. Unlike the MNIST perturbations, we cannot generate infinitely many perturbed datapoints, and so evaluations are performed on a fixed test set. Specific architecture, training, and evaluation details can be found in Appendix D.1.

We begin by training the CVAE on pairs (x, \tilde{x}) where x is an original image and \tilde{x} is a corrupted version of x , and compare it to training on less structured pairs where (x, \tilde{x}) are potentially both corruptions of the same image. The result, which is tabulated in Table 5 of Appendix D.2, is that

²We note that this is not the original intended use of the dataset, which was proposed as a general measure of robustness that should not be directly fitted. Nonetheless, it is a useful setting for learning perturbations.



Figure 2: Pairs of MI scenes (left) and their adversarial lighting perturbations (right).

conditioning on the original image learns a perturbation set with significantly better quality metrics. We additionally find that the latent space has semantic structure, where latent perturbations can be separated into their semantic types by their ℓ_2 norm as visualized in Figure 5 of Appendix D.3. The latent space can also generate reasonable interpolations and random samples, with several examples plotted in Figure 1 and additional examples in Appendix D.3. In total, these examples demonstrate how the perturbation set has learned a meaningful latent structure with reasonable combinations and variations of corruptions that have not been explicitly seen.

Adversarial training and randomized smoothing We employ the perturbation set in adversarial training and randomized smoothing to learn models which are robust against worst-case CIFAR10 common corruptions. We measure results at three radius thresholds $\{2.7, 3.9, 10.2\}$ which correspond to the 25th, 50th, and 75th percentiles of latent encodings as described in Appendix D.3. We compare to two data augmentation baselines of training on either perturbed data or samples drawn from the learned perturbation set, and also evaluate performance on three extra out-of-distribution corruptions (one for each weather, blur, and digital category) that are not present during training as described in Appendix D.

Table 1 summarizes the empirical results, where we first find that training with the CVAE perturbation set can improve generalization performance. Specifically, using the CVAE perturbation set to do data augmentation or adversarial training achieves 3 – 5% improved accuracy over pure data augmentation on all non-adversarial metrics, resulting in 95% clean, 90% perturbed, and 90% out of distribution accuracy. These gains in generalization motivate learning perturbation sets beyond the setting of worst-case robustness. Additionally, the CVAE perturbation set also improves worst-case performance, with the adversarially trained model being the most robust at 66% robust accuracy for $\epsilon = 3.9$ whereas pure data augmentation only achieves 17.8% robust accuracy. Several adversarial examples are shown in Figure 1, with additional examples plotted in Figure 9 of Appendix D.4.

Table 7 in Appendix D.5 summarizes the certified results using randomized smoothing, where the key points are that smoothing can further improve perturbed accuracy while obtaining non-trivial provable guarantees against common corruptions. We find that smoothing with smaller noise levels can achieve 92.6% perturbed accuracy, which is 2% higher than the best empirical approach from Table 1. Furthermore, with larger noise levels we can certify 39% accuracy at $\epsilon = 3.9$. Due to the semantic latent structure, this translates to guarantees against defocus blur and jpeg compression. Complete certification curves and further details concerning the certification procedure are in Appendix D.5.

5.3 Multi-illumination

Our last set of experiments looks at learning a perturbation set of multiple lighting conditions using the Multi-Illumination (MI) dataset [Murmann et al., 2019]. These consist of a thousand scenes captured in the wild under 25 different lighting variations, and our goal is to learn a perturbation set which captures these different lighting conditions. Since the process of learning lighting variations is largely similar to the image corruptions setting, we summarize the main robustness results at the MIP5 resolution (125×187), and defer further details and perturbation sets for higher resolutions to Appendix E.1. We show several adversarial examples from the learned perturbation set in Figure 2, with more adversarial examples, random samples, and interpolations in Appendix E.2.

Robustness to lighting perturbations We study the task of robustly generating material segmentation maps using a standard UNet architecture, with the main empirical results summarized in Table 10 in Appendix E.3. Robustness of the material prediction for each pixel is reported at the maximum radius $\epsilon = 17$ as well as the 50th and 75th percentiles $\epsilon \in \{7.35, 8.81\}$, where we find that adversarial training with the CVAE perturbation set improves robustness to worst-case lighting perturbations, achieving 35.4% robust accuracy at $\epsilon = 17$. We additionally train a certifiably robust network with

randomized smoothing, which obtains 30.7% perturbed accuracy and 12.4% certified accuracy at $\epsilon = 7.35$. Additional details and discussion of these results are in Appendix E.3.

6 Conclusion

In this paper, we presented a general framework for learning perturbation sets from data when the perturbation cannot be mathematically-defined. We outlined deterministic and probabilistic properties that measure the quality of these perturbation sets, the necessary subset and sufficient likelihood properties, which measure how well a perturbation set fits perturbed data. We then formally proved that a perturbation set based upon the CVAE framework satisfies these properties, resulting in a theoretically grounded approach that requires little tuning and is broadly applicable. The resulting learned perturbation sets can be used to empirically improve average and worst case robustness as well as generate provable robustness certificates on downstream tasks such as common image corruptions and lighting perturbations. Our work opens a pathway for practitioners to learn machine learning models that are robust to targeted, real-world perturbations that can be collected as data.

Broader Impact

One of the most important impacts of this work is to make the advancements in robust machine learning more accessible towards real-world scenarios. A common critique of the typical defenses in adversarial machine learning is their focus on small ℓ_p norm-bounded perturbations, which tend to be quite far from real-world adversarial attacks and have detrimental effects on standard performance. Existing applications of robust training to more real-world problems have been correspondingly limited to these highly constrained threat models in restricted settings [Salman et al., 2020, Wong et al., 2020]. By presenting a simple and general framework for learning threat models, we show that techniques from adversarial learning can be targeted to specific types of real-world applications and can sometimes even improve standard generalization performance. This bridges an important gap, and allows practitioners to begin to use robust training to learn robustness to the specific perturbations in their unique settings.

Beyond the image domains considered in this paper, this work could broadly apply to other domains such as audio (e.g. learning a perturbation set of structured background noise from weather or traffic, or differences in intonation of the same word or sentence between people) or in engineering and manufacturing (e.g. learning to model inaccuracies in the performance of a robot or machine performing a task). While this is good for the research field, more ethically gray applications of machine learning can also profit from this work. For example, facial recognition software is not universally viewed as a social positive, but could potentially be improved to be more robust to head poses, accessories, or environmental factors. In this work, we aimed to demonstrate with our experiments that perturbation learning can be broadly applied to more benign tasks.

Careful attention must be made to avoid a potential negative impact of learning underspecified threat models for adversarial machine learning. It may be possible for deficiencies in the data or training process to cause a threat model learned from data to not accurately capture the desired perturbation, especially if the criteria posed in Section 3.1 are not met or do not generalize. Such a threat model could lead to a false sense of robustness, which remains a common theme across defenses for even the well-defined ℓ_p threat model. It may also be possible to adversarially subvert the metrics used for measuring the quality of a perturbation set, producing a compromised threat model which appears to be reasonable. Special care must be taken when evaluating threat models which are learned from data, while claims and specifications of the threat model need to be carefully stated in order to avoid repeating the past mistakes of adversarially robust machine learning.

References

- M. Alzantot, Y. Sharma, A. Elgohary, B.-J. Ho, M. Srivastava, and K.-W. Chang. Generating natural language adversarial examples. *arXiv preprint arXiv:1804.07998*, 2018.
- A. Athalye, L. Engstrom, A. Ilyas, and K. Kwok. Synthesizing robust adversarial examples. *arXiv preprint arXiv:1707.07397*, 2017.

- A. Bhattad, M. J. Chong, K. Liang, B. Li, and D. Forsyth. Unrestricted adversarial examples via semantic manipulation. In *International Conference on Learning Representations*, 2020.
- B. Biggio, I. Corona, D. Maiorca, B. Nelson, N. Šrndić, P. Laskov, G. Giacinto, and F. Roli. Evasion attacks against machine learning at test time. In *Joint European conference on machine learning and knowledge discovery in databases*, pages 387–402. Springer, 2013.
- Y. Cao, C. Xiao, D. Yang, J. Fang, R. Yang, M. Liu, and B. Li. Adversarial objects against lidar-based autonomous driving systems. *arXiv preprint arXiv:1907.05418*, 2019.
- N. Carlini, A. Athalye, N. Papernot, W. Brendel, J. Rauber, D. Tsipras, I. Goodfellow, A. Madry, and A. Kurakin. On evaluating adversarial robustness. *arXiv preprint arXiv:1902.06705*, 2019.
- J. M. Cohen, E. Rosenfeld, and J. Z. Kolter. Certified adversarial robustness via randomized smoothing. *arXiv preprint arXiv:1902.02918*, 2019.
- F. Croce and M. Hein. Provable robustness against all adversarial l_p -perturbations for $p \geq 1$. *arXiv preprint arXiv:1905.11213*, 2019.
- E. D. Cubuk, B. Zoph, D. Mane, V. Vasudevan, and Q. V. Le. Autoaugment: Learning augmentation strategies from data. In *Proceedings of the IEEE conference on computer vision and pattern recognition*, pages 113–123, 2019.
- T. DeVries and G. W. Taylor. Improved regularization of convolutional neural networks with cutout. *arXiv preprint arXiv:1708.04552*, 2017.
- L. Engstrom, D. Tsipras, L. Schmidt, and A. Madry. A rotation and a translation suffice: Fooling cnns with simple transformations. *arXiv preprint arXiv:1712.02779*, 1(2):3, 2017.
- K. Eykholt, I. Evtimov, E. Fernandes, B. Li, A. Rahmati, C. Xiao, A. Prakash, T. Kohno, and D. Song. Robust physical-world attacks on deep learning visual classification. In *Proceedings of the IEEE Conference on Computer Vision and Pattern Recognition*, pages 1625–1634, 2018.
- R. Geirhos, P. Rubisch, C. Michaelis, M. Bethge, F. A. Wichmann, and W. Brendel. Imagenet-trained cnns are biased towards texture; increasing shape bias improves accuracy and robustness. *arXiv preprint arXiv:1811.12231*, 2018.
- I. J. Goodfellow, J. Shlens, and C. Szegedy. Explaining and harnessing adversarial examples. *arXiv preprint arXiv:1412.6572*, 2014.
- S. Gowal, K. Dvijotham, R. Stanforth, R. Bunel, C. Qin, J. Uesato, R. Arandjelovic, T. Mann, and P. Kohli. On the effectiveness of interval bound propagation for training verifiably robust models. *arXiv preprint arXiv:1810.12715*, 2018.
- S. Gowal, C. Qin, P.-S. Huang, T. Cemgil, K. Dvijotham, T. Mann, and P. Kohli. Achieving robustness in the wild via adversarial mixing with disentangled representations. *arXiv preprint arXiv:1912.03192*, 2019.
- K. He, X. Zhang, S. Ren, and J. Sun. Identity mappings in deep residual networks. In *European conference on computer vision*, pages 630–645. Springer, 2016.
- D. Hendrycks and T. Dietterich. Benchmarking neural network robustness to common corruptions and perturbations. *arXiv preprint arXiv:1903.12261*, 2019.
- D. Hendrycks, N. Mu, E. D. Cubuk, B. Zoph, J. Gilmer, and B. Lakshminarayanan. Augmix: A simple data processing method to improve robustness and uncertainty. *arXiv preprint arXiv:1912.02781*, 2019.
- M. Jaderberg, K. Simonyan, A. Zisserman, et al. Spatial transformer networks. In *Advances in neural information processing systems*, pages 2017–2025, 2015.
- R. Jia, A. Raghunathan, K. Göksel, and P. Liang. Certified robustness to adversarial word substitutions. *arXiv preprint arXiv:1909.00986*, 2019.

- D. P. Kingma and J. Ba. Adam: A method for stochastic optimization. *arXiv preprint arXiv:1412.6980*, 2014.
- A. Kurakin, I. Goodfellow, and S. Bengio. Adversarial machine learning at scale. *arXiv preprint arXiv:1611.01236*, 2016.
- C. Laidlaw and S. Feizi. Functional adversarial attacks. In *Advances in Neural Information Processing Systems*, pages 10408–10418, 2019.
- J. Li, S. Qu, X. Li, J. Szurley, J. Z. Kolter, and F. Metze. Adversarial music: Real world audio adversary against wake-word detection system. In *Advances in Neural Information Processing Systems*, pages 11908–11918, 2019a.
- J. B. Li, F. R. Schmidt, and J. Z. Kolter. Adversarial camera stickers: A physical camera attack on deep learning classifier. *arXiv preprint arXiv:1904.00759*, 2019b.
- A. Madry, A. Makelov, L. Schmidt, D. Tsipras, and A. Vladu. Towards deep learning models resistant to adversarial attacks. *arXiv preprint arXiv:1706.06083*, 2017.
- P. Maini, E. Wong, and J. Z. Kolter. Adversarial robustness against the union of multiple perturbation models. *arXiv preprint arXiv:1909.04068*, 2019.
- C. Michaelis, B. Mitzkus, R. Geirhos, E. Rusak, O. Bringmann, A. S. Ecker, M. Bethge, and W. Brendel. Benchmarking robustness in object detection: Autonomous driving when winter is coming. *arXiv preprint arXiv:1907.07484*, 2019.
- T. Miyato, A. M. Dai, and I. Goodfellow. Adversarial training methods for semi-supervised text classification. *arXiv preprint arXiv:1605.07725*, 2016.
- L. Murmann, M. Gharbi, M. Aittala, and F. Durand. A dataset of multi-illumination images in the wild. In *Proceedings of the IEEE International Conference on Computer Vision*, pages 4080–4089, 2019.
- A. Raghunathan, J. Steinhardt, and P. Liang. Certified defenses against adversarial examples. *arXiv preprint arXiv:1801.09344*, 2018.
- L. Rice, E. Wong, and J. Z. Kolter. Overfitting in adversarially robust deep learning. *arXiv preprint arXiv:2002.11569*, 2020.
- A. Robey, H. Hassani, and G. J. Pappas. Model-based robust deep learning. *arXiv preprint arXiv:2005.10247*, 2020.
- O. Ronneberger, P. Fischer, and T. Brox. U-net: Convolutional networks for biomedical image segmentation. In *International Conference on Medical image computing and computer-assisted intervention*, pages 234–241. Springer, 2015.
- E. Rusak, L. Schott, R. Zimmermann, J. Bitterwolf, O. Bringmann, M. Bethge, and W. Brendel. Increasing the robustness of dnns against image corruptions by playing the game of noise. *arXiv preprint arXiv:2001.06057*, 2020.
- S. Sagawa, P. W. Koh, T. B. Hashimoto, and P. Liang. Distributionally robust neural networks for group shifts: On the importance of regularization for worst-case generalization. *arXiv preprint arXiv:1911.08731*, 2019.
- H. Salman, M. Sun, G. Yang, A. Kapoor, and J. Z. Kolter. Black-box smoothing: A provable defense for pretrained classifiers. *arXiv preprint arXiv:2003.01908*, 2020.
- M. Sharif, S. Bhagavatula, L. Bauer, and M. K. Reiter. A general framework for adversarial examples with objectives. *ACM Transactions on Privacy and Security (TOPS)*, 22(3):1–30, 2019.
- A. Sinha, H. Namkoong, and J. Duchi. Certifying some distributional robustness with principled adversarial training. *arXiv preprint arXiv:1710.10571*, 2017.
- L. N. Smith. Cyclical learning rates for training neural networks. In *2017 IEEE Winter Conference on Applications of Computer Vision (WACV)*, pages 464–472. IEEE, 2017.

- K. Sohn, H. Lee, and X. Yan. Learning structured output representation using deep conditional generative models. In *Advances in neural information processing systems*, pages 3483–3491, 2015.
- Y. Song, R. Shu, N. Kushman, and S. Ermon. Constructing unrestricted adversarial examples with generative models. In *Advances in Neural Information Processing Systems*, pages 8312–8323, 2018.
- D. Stutz, M. Hein, and B. Schiele. Confidence-calibrated adversarial training and detection: More robust models generalizing beyond the attack used during training. *arXiv preprint arXiv:1910.06259*, 2019.
- C. Szegedy, W. Zaremba, I. Sutskever, J. Bruna, D. Erhan, I. Goodfellow, and R. Fergus. Intriguing properties of neural networks. *arXiv preprint arXiv:1312.6199*, 2013.
- F. Tramèr and D. Boneh. Adversarial training and robustness for multiple perturbations. In *Advances in Neural Information Processing Systems*, pages 5858–5868, 2019.
- E. Wong and J. Z. Kolter. Provable defenses against adversarial examples via the convex outer adversarial polytope. *arXiv preprint arXiv:1711.00851*, 2017.
- E. Wong, F. Schmidt, J. H. Metzen, and J. Z. Kolter. Scaling provable adversarial defenses. In *Advances in Neural Information Processing Systems*, pages 8400–8409, 2018.
- E. Wong, F. R. Schmidt, and J. Z. Kolter. Wasserstein adversarial examples via projected sinkhorn iterations. *arXiv preprint arXiv:1902.07906*, 2019.
- E. Wong, T. Schneider, J. Schmitt, F. R. Schmidt, and J. Z. Kolter. Neural network virtual sensors for fuel injection quantities with provable performance specifications. In *2020 IEEE Intelligent Vehicles Symposium (IV)*. IEEE, 2020.
- C. Xiao, B. Li, J.-Y. Zhu, W. He, M. Liu, and D. Song. Generating adversarial examples with adversarial networks. *arXiv preprint arXiv:1801.02610*, 2018a.
- C. Xiao, J.-Y. Zhu, B. Li, W. He, M. Liu, and D. Song. Spatially transformed adversarial examples. *arXiv preprint arXiv:1801.02612*, 2018b.
- G. Yang, T. Duan, E. Hu, H. Salman, I. Razenshteyn, and J. Li. Randomized smoothing of all shapes and sizes. *arXiv preprint arXiv:2002.08118*, 2020.
- S. Zagoruyko and N. Komodakis. Wide residual networks. *arXiv preprint arXiv:1605.07146*, 2016.
- H. Zhang, M. Cisse, Y. N. Dauphin, and D. Lopez-Paz. mixup: Beyond empirical risk minimization. *arXiv preprint arXiv:1710.09412*, 2017.
- H. Zhang, H. Chen, C. Xiao, B. Li, D. Boning, and C.-J. Hsieh. Towards stable and efficient training of verifiably robust neural networks. *arXiv preprint arXiv:1906.06316*, 2019.

A Theoretical results

In this section, we present the theoretical results in their full detail and exposition. Both of the main theorems presented in this work require a number of preceding results in order to formally link the prior and the posterior distribution based on their KL divergence. We will present and prove these supporting results before proving each main theorem.

A.1 Proof of Theorem 1

Theorem 1 connects the CVAE objective to the necessary subset property. In order to prove this, we first prove three supporting lemmas. Lemma 1 states that if the expected value of a function over a normal distribution is low, then for any fixed radius there must exist a point within the radius with proportionally low function value. This leverages the fact that the majority of the probability mass is concentrated around the mean and can be characterized by the Mahalanobis distance.

Lemma 1. *Let $f(u) : \mathbb{R}^k \rightarrow \mathbb{R}_+$ be a non-negative integrable function, and let $\mathcal{N}_k(0, I)$ be a k -dimensional standard multivariate normal random variable with zero mean and identity covariance. Suppose $\mathbb{E}_{u \sim \mathcal{N}(0, I)}[f(u)] \leq \delta$ for some $\delta > 0$. Then, for any pair (r, α) where r is the Mahalanobis distance which captures $1 - \alpha$ of the probability mass of $\mathcal{N}_k(0, I)$, there exists a u such that $\|u\|_2 \leq r$ and $f(u) \leq \frac{\delta}{1 - \alpha}$.*

Proof. We will prove this by contradiction. Assume for sake of contradiction that for all u such that $\|u\|_2 \leq r$, we have $f(u) > \frac{\delta}{1 - \alpha}$. We divide the expectation into two integrals over the inside and outside of the Mahalanobis ball:

$$\mathbb{E}_{u \sim \mathcal{N}(0, I)} [f(u)] = \int_{\|u\|_2 \leq r} f(u)p(u)du + \int_{\|u\|_2 > r} f(u)p(u)du \quad (7)$$

Using the assumption on the first integral and non-negativity of f in the second integrand, we can conclude

$$\mathbb{E}_{u \sim \mathcal{N}(0, I)} [f(u)] > \int_{\|u\|_2 \leq r} \frac{\delta}{1 - \alpha} p(u)du = \delta \quad (8)$$

where the equality holds by definition of the Mahalanobis distance, which contradicts the initial assumption that $\mathbb{E}_{u \sim \mathcal{N}(0, I)} [f(u)] \leq \delta$. Thus, we have proven by contradiction that there exists a u such that $\|u\|_2 \leq r$ and $f(u) \leq \frac{\delta}{1 - \alpha}$. \square

Our second lemma, Lemma 2, is an important result that comes from the algebraic form of the KL divergence. It is needed to connect the bound on the KL divergence to the actual variances of the prior and the posterior distribution, and uses the LambertW function to do so.

Lemma 2. *Let W_k be the LambertW function with branch k . Let $x > 0$, and suppose $x - \log x \leq y$. Then, $x \in [a, b]$ where $a = -W_0(-e^{-y})$ and $b = -W_{-1}(-e^{-y})$. Additionally, these bounds coincide at $x = 1$ when $y = 1$.*

Proof. The LambertW function $W_k(y)$ is defined as the inverse function of $y = xe^x$, where the path to multiple solutions is determined by the branch k . We can then write the inverse of $y = x - \log x$ as one of the following two solutions:

$$x \in \{-W_0(-e^{-y}), -W_{-1}(-e^{-y})\} \quad (9)$$

Since $x - \log x$ is convex with minimum at $x = 1$, and since the two solutions surround $x = 1$, the set of points which satisfy $x - \log x \leq y$ is precisely the interval $[-W_0(-e^{-y}), -W_{-1}(-e^{-y})]$. Evaluating the bound at $y = 1$ completes the proof. \square

Lemma 3 is the last lemma needed to prove Theorem 1, which explicitly bounds terms involving the mean and variance of the prior and posterior distributions by their KL distance, leveraging Lemma 2 to bound the ratio of the variances. The two quantities bounded in this lemma will be used in the main theorem to bound the distance of a point with low reconstruction error from the prior distribution.

Lemma 3. Suppose the KL distance between two normals is bounded, so $KL(\mathcal{N}(\mu_1, \sigma_1^2) \parallel \mathcal{N}(\mu_2, \sigma_2^2)) \leq K$ for some constant K . Then,

$$(\mu_1 - \mu_2)^2 \frac{1}{\sigma_2^2} \leq K$$

and also $\frac{\sigma_1^2}{\sigma_2^2} \in [a, b]$ where

$$a = -W_0(-e^{-(K+1)}), \quad b = -W_{-1}(-e^{-(K+1)})$$

Proof. By definition of KL divergence, we have

$$\frac{\sigma_1^2}{\sigma_2^2} + (\mu_1 - \mu_2)^2 \frac{1}{\sigma_2^2} - 1 - \log \frac{\sigma_1^2}{\sigma_2^2} \leq K \quad (10)$$

Since $x - \log x \geq 1$ for $x \geq 0$, we apply this for $x = \frac{\sigma_1^2}{\sigma_2^2}$ to prove the first bound on the squared distance as

$$(\mu_1 - \mu_2)^2 \frac{1}{\sigma_2^2} \leq K \quad (11)$$

Next, since $(\mu_1 - \mu_2)^2 \frac{1}{\sigma_2^2} \geq 0$, we can bound the remainder as the following

$$\frac{\sigma_1^2}{\sigma_2^2} - \log \frac{\sigma_1^2}{\sigma_2^2} \leq K + 1 \quad (12)$$

and using Lemma 2, we can bound $\frac{\sigma_1^2}{\sigma_2^2} \in [a, b]$ where

$$a = -W_0(-e^{-(K+1)}), \quad b = -W_{-1}(-e^{-(K+1)})$$

□

With these three results, we can now prove the first main theorem, which we is presented below in its complete form, allowing us to formally tie the CVAE objective to the existence of a nearby point with low reconstruction error.

Theorem 1. Consider the likelihood lower bound for $x \in \mathbb{R}^n$ from the conditional VAE in k -dimensional latent space conditioned on some other input y . Let the posterior, prior, and decoder distributions be standard multivariate normals with diagonal covariance as follows

$$q(z|x, y) \sim \mathcal{N}(\mu(x, y), \sigma^2(x, y)), \quad p(z|y) \sim \mathcal{N}(\mu(y), \sigma^2(y)), \quad p(x|z, y) \sim \mathcal{N}(g(z, y), I)$$

resulting in the following likelihood lower bound:

$$\log p(x|y) \geq \mathbb{E}_{q(z|x, y)}[\log p(x|z, y)] - KL(q(z|x, y) \parallel p(z|y)) \quad (13)$$

Suppose we have trained the lower bound to some thresholds R, K_i

$$\mathbb{E}_{q(z|x, y)}[\log p(x|z, y)] \geq R, \quad KL(q(z|x, y) \parallel p(z|y)) \leq \sum_{i=1}^k K_i$$

where K_i bounds the KL-divergence of the i th dimension. Let r be the Mahalanobis distance which captures $1 - \alpha$ of the probability mass for a k -dimensional standard multivariate normal for some $0 < \alpha < 1$. Then, there exists a z such that $\| \frac{z - \mu(y)}{\sigma(y)} \|_2 \leq \epsilon$ and $\|g(z, y) - x\|_2^2 \leq \delta$ for

$$\epsilon = Br + \sqrt{\sum_i K_i}, \quad \delta = -\frac{1}{1 - \alpha} (2R + m \log(2\pi))$$

where B is a constant dependent on K_i . Moreover, as $R \rightarrow -\frac{1}{2}m \log(2\pi)$ and $K_i \rightarrow 0$ (the theoretical limits of these bounds, e.g. by training), then $\epsilon \rightarrow r$ and $\delta \rightarrow 0$.

Proof. The high level strategy for this proof will consist of two main steps. First, we will show that there exists a point near the encoding distribution which has low reconstruction error, where we leverage the Mahalanobis distance to capture nearby points with Lemma 1. Then, we apply the triangle inequality to bound its distance under the prior encoding. Finally, we will use Lemma 3 to bound remaining quantities relating the distances between the prior and encoding distributions to complete the proof.

Let $z(u) = u \cdot \sigma(x, y) + \mu(x, y)$ be the parameterization trick of the encoding distribution. Rearranging the log probability in the assumption and using the reparameterization trick, we get

$$\mathbb{E}_u [\|x - g(z(u), y)\|_2^2] \leq -2R - m \log(2\pi) = \delta(1 - \alpha) \quad (14)$$

Applying Lemma 1, there must exist a u such that $\|u\| \leq r$ and $\|x - g(z(u), y)\|_2^2 \leq \delta$, and so $z(u)$ satisfies the reconstruction criteria for δ . We will now show that $z(u)$ fulfills the remaining criteria for ϵ : calculating its ℓ_2 norm under the prior distribution and applying the triangle inequality, we get

$$\left\| \frac{z(u) - \mu(y)}{\sigma(y)} \right\|_2 = \left\| \frac{u \cdot \sigma(x, y) + \mu(x, y) - \mu(y)}{\sigma(y)} \right\|_2 \leq \left\| \frac{u \cdot \sigma(x, y)}{\sigma(y)} \right\|_2 + \left\| \frac{\mu(x, y) - \mu(y)}{\sigma(y)} \right\|_2 \quad (15)$$

We can use Lemma 3 on the KL assumption to bound the following quantities

$$(\mu_i(y) - \mu_i(x, y))^2 \frac{1}{\sigma_i^2(y)} \leq K_i, \quad \frac{\sigma_i^2(x, y)}{\sigma_i^2(y)} \in [a_i, b_i] \quad (16)$$

where $[a_i, b_i]$ are as defined from Lemma 3.

Let $B = \max_i \sqrt{b_i}$, so $\frac{\sigma_i(x, y)}{\sigma_i(y)} \leq B$ for all i . Plugging this in along with the previous bounds we get the following bound on the norm of $z(u)$ before the prior reparameterization:

$$\left\| \frac{z(u) - \mu(y)}{\sigma(y)} \right\|_2 \leq Br + \sqrt{\sum_i K_i} = \epsilon \quad (17)$$

Thus, the norm (before the prior reparameterization) and reconstruction error of $z(u)$ can be bounded by ϵ and δ .

To conclude the proof, we note that from Lemma 2, $K_i \rightarrow 0$ for all i implies $B \rightarrow 1$, and so $\epsilon \rightarrow r$. Similarly by inspection, $R \rightarrow -\frac{1}{2}m \log(2\pi)$ implies that $\delta \rightarrow 0$, which concludes the proof. \square

A.2 Proof of Theorem 2

In this section, we move on to prove the second main result of this paper, Theorem 2, which connects the CVAE objective to the sufficient likelihood property. The proof for this theorem is not immediate, because since the generator is an arbitrary function, two normal distributions which have a difference in means have an exponentially growing ratio in their tail distributions, and so truncating the normal distributions is crucial. This truncation is leveraged in Lemma 4, which bounds the ratio of two normal distributions constrained within an ℓ_2 ball, and is what allows us to connect the expectation over the prior with the expectation over the posterior.

Lemma 4. *Let $p \sim \mathcal{N}(0, 1)$ and $q \sim \mathcal{N}(-\mu/\sigma^2, 1/\sigma^2)$. Then,*

$$\frac{q(z)}{p(z)} \mathbf{1}(|\sigma z + \mu| \leq r) \leq h(r, \mu, \sigma). \quad (18)$$

Furthermore if $\mu^2 \leq K$ and $\sigma \in [a, b]$, then $h(r, \mu, \sigma) \leq b e^{\max(C_1, C_2)}$ where

$$C_1 = (b^2 - 1)r^2 - K, \quad C_2 = \frac{1}{a^2} \left((1 - a^2)r^2 + 2r\sqrt{K} + K \right).$$

Proof. The proof here is almost purely algebraic in nature. By definition of q and p , we have

$$\frac{q(z)}{p(z)} = \sigma e^{-\frac{1}{2}((\sigma z + \mu)^2 - z^2)} = \sigma e^{\frac{1}{2}((1 - \sigma^2)z^2 - 2\sigma\mu z - \mu^2)} \quad (19)$$

We will focus on bounding the exponent, $(1 - \sigma^2)z^2 - 2\sigma\mu z - \mu^2$. We can bound this by considering two cases. First, suppose that $1 - \sigma^2 < 0$ and so the exponent is a concave quadratic. Then, the maximum value of the quadratic is at its root:

$$2(1 - \sigma^2)z - 2\sigma\mu = 0 \Rightarrow z = \frac{\sigma\mu}{1 - \sigma^2} \quad (20)$$

Further assume that this z is within the interval of the indicator function, so $\left| \frac{\sigma^2\mu}{1 - \sigma^2} + \mu \right| = \left| \frac{\mu}{1 - \sigma^2} \right| \leq r$. Then, plugging in the maximum value into the quadratic results in the following bound f_1 for this case:

$$(1 - \sigma^2)z^2 - 2\sigma\mu z - \mu^2 \leq -(1 - \sigma^2) \frac{\sigma^2\mu^2}{(1 - \sigma^2)^2} - \mu^2 \leq (\sigma^2 - 1)r^2 - \mu^2 \equiv f_1(r, \mu, \sigma) \quad (21)$$

Consider the other case, so either $1 - \sigma^2 \geq 0$, or the optimal value for z^* in the previous case when $1 - \sigma^2 < 0$ is not within the interval $|\sigma z + \mu| \leq r$. Then, the maximum value of this quadratic must occur at $|\sigma z + \mu| = r$, so $z = \frac{\pm r - \mu}{\sigma}$. Plugging this into the quadratic for positive r , this results in

$$(1 - \sigma^2)z^2 - 2\sigma\mu z - \mu^2 \Big|_{\sigma z + \mu = r} = \frac{1}{\sigma^2} \left((1 - \sigma^2)r^2 - 2r\mu + \mu^2 \right) \quad (22)$$

and for negative r , this is

$$(1 - \sigma^2)z^2 - 2\sigma\mu z - \mu^2 \Big|_{\sigma z + \mu = -r} = \frac{1}{\sigma^2} \left((1 - \sigma^2)r^2 + 2r\mu + \mu^2 \right) \quad (23)$$

and so we can bound this case with the following function f_2 :

$$(1 - \sigma^2)z^2 - 2\sigma\mu z - \mu^2 \leq \frac{1}{\sigma^2} \left((1 - \sigma^2)r^2 + 2|r\mu| + \mu^2 \right) \equiv f_2(r, \mu, \sigma) \quad (24)$$

Plugging in the maximum over both cases forms our final bound on the ratio of distributions.

$$\frac{q(z)}{p(z)} \mathbb{1}(|\sigma z + \mu| \leq r) \leq \sigma e^{\max(f_1(r, \mu, \sigma), f_2(r, \mu, \sigma))} = h(r, \mu, \sigma) \quad (25)$$

To finish the proof, assume we have the corresponding bounds on μ and σ . Then, the first case can be bounded with C_1 defined as

$$f_1(r, \mu, \sigma) \leq (b^2 - 1)r^2 - K = C_1$$

The second case can be bounded with C_2 defined as

$$f_2(r, \mu, \sigma) \leq \frac{1}{a^2} \left((1 - a^2)r^2 + 2r\sqrt{K} + K \right) = C_2$$

And thus we can bound $h(r, \mu, \sigma)$ as

$$h(r, \mu, \sigma) \leq b e^{\max(C_1, C_2)} = H$$

□

Lemma 4 can be directly applied to the setting of Theorem 2 for the case of a non-conditional VAE with a standard normal distribution for the prior. However, since we are using conditional VAEs instead, the prior distribution has its own mean and variance and so the posterior distribution needs to be unparameterized from the posterior and reparameterized with the prior. Corollary 1 establishes this formally, extending Lemma 4 to the conditional setting.

Corollary 1. *Let $p \sim \mathcal{N}(0, 1)$ and $q \sim \mathcal{N}\left(\frac{\mu_2 - \mu_1}{\sigma_1}, \frac{\sigma_2^2}{\sigma_1^2}\right)$. Then,*

$$\frac{q(z)}{p(z)} \mathbb{1}\left(\left| \frac{\sigma_1 z + \mu_1 - \mu_2}{\sigma_2} \right| \leq r\right) \leq h(r, \mu, \sigma) \quad (26)$$

where $\mu = \frac{1}{\sigma_2}(\mu_1 - \mu_2)$ and $\sigma = \frac{\sigma_1}{\sigma_2}$. Furthermore, if $KL(\mathcal{N}(\mu_1, \sigma_1^2) \parallel \mathcal{N}(\mu_2, \sigma_2^2)) \leq K$ for some constant K , then $h(r, \mu, \sigma) \leq H$ where H is a constant which depends on K .

Proof. First, note that Lemma 3 implies that $\mu^2 \leq K$ and $\sigma \in [a, b]$. Observe that $q \sim \mathcal{N}\left(-\frac{\mu}{\sigma}, \frac{1}{\sigma^2}\right)$ and $\frac{\sigma_1 z + \mu_1 - \mu_2}{\sigma_2} = \sigma z + \mu$, and so the proof reduces to an application of Lemma 4 to this particular μ and σ . \square

These results allow us to bound the ratio of the prior and posterior distributions within a fixed radius, which will allow us to bound the expectation over the prior with the expectation over the posterior. We can now finally prove Theorem 2, presented in its complete form below.

Theorem 2. *Consider the likelihood lower bound for $x \in \mathbb{R}^n$ from the conditional VAE in k -dimensional latent space conditioned on some other input y . Let the posterior, prior, and decoder distributions be standard multivariate normals with diagonal covariance as follows*

$$q(z|x, y) \sim \mathcal{N}(\mu(x, y), \sigma^2(x, y)), \quad p(z|y) \sim \mathcal{N}(\mu(y), \sigma^2(y)), \quad p(x|z, y) \sim \mathcal{N}(g(z, y), I)$$

resulting in the following likelihood lower bound:

$$\log p(x|y) \geq \mathbb{E}_{q(z|x, y)}[\log p(x|z, y)] - KL(q(z|x, y)||p(z|y)) \quad (27)$$

Suppose we have trained the lower bound to some thresholds R, K_i

$$\mathbb{E}_{q(z|x, y)}[\log p(x|z, y)] \geq R, \quad KL(q(z|x, y)||p(z|y)) \leq \sum_{i=1}^k K_i$$

where K_i bounds the KL-divergence of the i th dimension. Let r be the Mahalanobis distance which captures $1 - \alpha$ of the probability mass for a k -dimensional standard multivariate normal for some $0 < \alpha < 1$. Then, the truncated expected reconstruction error can be bounded with

$$\mathbb{E}_{p_r(u)} [\|g(u \cdot \sigma(y) + \mu(y), y) - x\|_2^2] \leq -\frac{1}{1 - \alpha} (2R + m \log(2\pi)) H$$

where $p_r(u)$ is a multivariate normal that has been truncated to radius r and H is a constant that depends exponentially on K_i .

Proof. The overall strategy for this proof will be as follows. First, we will rewrite the expectation over a truncated normal into an expectation over a standard normal, using an indicator function to control the radius. Second, we will do an ‘‘unparameterization’’ of the standard normal to match the parameterized objective in the assumption. Finally, we will bound the ratio of the unparameterized density over the normal prior, which allows us to bound the expectation over the prior with the assumption. This last step to bound the ratio of densities is made possible by the truncation, which would otherwise grow exponentially with the tails of the distribution.

For notational simplicity, let $f(\cdot) = \|g(\cdot, y) - x\|_2^2$. The quantity we wish to bound can be rewritten using the Mahalanobis distance as

$$\mathbb{E}_{p_\alpha} [f(u \cdot \sigma(y) + \mu(y))] = \frac{1}{1 - \alpha} \int_u f(u \cdot \sigma(y) + \mu(y)) \mathbb{1}(\|u\| \leq r) p(u) dz \quad (28)$$

where we used the fact that $p_r(u) = \frac{1}{1 - \alpha} \mathbb{1}(\|u\| \leq r) p(u)$, which simply rewrites the density of a truncated normal using a scaled standard normal density and an indicator function. We can do a parameterization trick $z = u \cdot \sigma(y) + \mu(y)$ to rewrite this as

$$\mathbb{E}_{p_r} [f(u \cdot \sigma(y) + \mu(y))] = \frac{1}{1 - \alpha} \int_z f(z) \mathbb{1}\left(\left\|\frac{z - \mu(y)}{\sigma(y)}\right\| \leq r\right) p_{z|y}(z) dz \quad (29)$$

followed by a reverse parameterization trick with $v = \frac{z - \mu(x, y)}{\sigma(x, y)}$ to get the following equivalent expression

$$\frac{1}{1 - \alpha} \int_z f(v \cdot \sigma(x, y) + \mu(x, y)) \mathbb{1}\left(\left\|\frac{v \cdot \sigma(x, y) + \mu(x, y) - \mu(y)}{\sigma(y)}\right\| \leq r\right) p_v(v) dz \quad (30)$$

where $p_v \sim \mathcal{N}\left(\frac{\mu(x) - \mu(x, y)}{\sigma(x, y)}, \frac{\sigma^2(x)}{\sigma^2(x, y)}\right)$. For convenience, we can let

$$\hat{p}_v(v) = \mathbb{1}\left(\left\|\frac{v \cdot \sigma(x, y) + \mu(x, y) - \mu(y)}{\sigma(y)}\right\| \leq r\right) p_v(v)$$

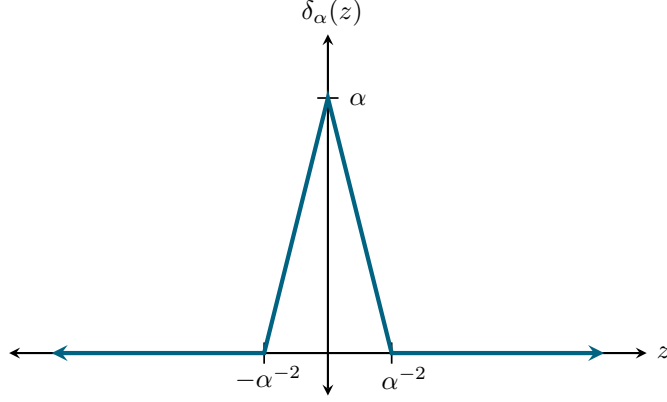


Figure 3: A simple example demonstrating how the expected value of a function can tend to zero while the maximum tends to infinity as $a \rightarrow \infty$.

which can be interpreted as a truncated version of p_v , and so the expectation can be represented more succinctly as

$$\mathbb{E}_{p_r} [f(u \cdot \sigma(y) + \mu(y))] = \frac{1}{1 - \alpha} \int_z f(v \cdot \sigma(x, y) + \mu(x, y)) \hat{p}_v(v) dz. \quad (31)$$

We will now bound $\hat{p}_v(v)$ with the standard normal distribution $p(v)$ so that we can apply our assumption. Because f is non-negative, the ℓ_2 constraint in $\hat{p}_v(v)$ can be relaxed to an element-wise ℓ_∞ constraint to get

$$\hat{p}_v(v) \leq p(v) \prod_{i=1}^k \mathbb{1} \left(\left| \frac{v \cdot \sigma(x, y) + \mu(x, y) - \mu(y)}{\sigma(y)} \right| \leq r \right) \frac{p_v(v_i)}{p(v_i)} \quad (32)$$

where we also used the fact that p is a diagonal normal, so $\prod_{i=1}^k p(v_i) = p(v)$. Each term in this product can be bounded by Lemma 4 to get

$$\hat{p}_v(v) \leq p(v) \prod_{i=1}^k H_i = p(v) \cdot H \quad (33)$$

where H_i is as defined in Corollary 1 for each i using the corresponding K_i , and we let $H = \prod_{i=1}^k H_i$. Thus we can now bound the truncated expected value by plugging in our bound for $\hat{p}_v(v)$ into Equation (31) to get

$$\mathbb{E}_{p_r} [f(u \cdot \sigma(y) + \mu(y))] \leq \frac{H}{1 - \alpha} \cdot \mathbb{E}_{q(z|x,y)} [f(z)] \quad (34)$$

Using our lower bound on the expected log likelihood from the assumption, we can bound the remaining integral with

$$\mathbb{E}_{q(z|x,y)} [f(z)] \leq -2R - m \log(2\pi) \quad (35)$$

and so combining this into our previous bound from Equation (34) results in the final bound

$$E_{p_r} [f(u)] \leq -\frac{1}{1 - \alpha} (2R + m \log(2\pi)) H \quad (36)$$

□

A.3 Discussion of theoretical results

We first note that the bound on the expected reconstruction error in Theorem 2 is larger than the corresponding bound from Theorem 1 by an exponential factor. This gap is to some extent desired, since Theorem 1 characterizes the existence of a highly accurate approximation whereas Theorem 2 characterizes the average case, and so if this gap were too small, the average case of allowable

perturbations would be constrained in reconstruction error, which is not necessarily desired in all settings.

This relates to the overapproximation error, or the maximum reconstruction error within the perturbation set. Initially one may think that having low overapproximation error to be a desirable property of perturbation sets, in order to constrain the perturbation set from deviating by “too much.” However, perturbation sets such as the rotation-translation-skew perturbations for MNIST will always have high overapproximation error, and so reducing this is not necessarily desired. Furthermore, it is not theoretically guaranteed for the CVAE to minimize the overapproximation error without further assumptions. This is because it is possible for a function to be arbitrarily small in expectation but be arbitrarily high at some nearby point, so optimizing the CVAE objective does not imply low overapproximation error. A simple concrete example demonstrating this is the following piecewise linear function

$$\delta_a(z) = \begin{cases} a^3z + a & \text{for } -\frac{1}{a^2} \leq z < 0 \\ -a^3z + a & \text{for } 0 \leq z < \frac{1}{a^2} \\ 0 & \text{otherwise} \end{cases}$$

for $a > 0$ as seen in Figure 3. Note that $\max_{|z| \leq \epsilon} \delta_a(z) = a$ which is unbounded as $a \rightarrow \infty$ for all $\epsilon \geq 0$, while at the same time $\mathbb{E}_{\mathcal{N}(0,1)}[\delta_a(z)] \leq \frac{1}{a} \rightarrow 0$. Thus, explicitly minimizing overapproximation error is not necessarily desired nor is it guaranteed by the CVAE. Nonetheless, we report it anyways to give the reader a sense of how much the CVAE can deviate within the learned perturbation set.

B Evaluating a perturbation set

In this section we describe in more detail the process of selecting a radius for a learned perturbation set and formally describe all the details regarding the evaluation metrics for a perturbation set learned with a CVAE. As a reminder, let $\mu(x, \tilde{x}), \sigma(x, \tilde{x})$ be the posterior encoding, $\mu(x), \sigma(x)$ be the prior encoding, and $g(x, z)$ be the decoder for the CVAE. We will use u to represent the latent space before the parameterization trick. Then the perturbation set defined by our generative process is

$$\mathcal{S}(x) = \{g(z, x) : z = u \cdot \sigma(x) + \mu(x), \|u\| \leq \epsilon\}$$

and the probabilistic perturbation set is defined by the truncated normal distribution \mathcal{N}_ϵ before the parameterization trick as follows,

$$\mathcal{S}(x) \sim \text{Normal}(g(z, x), I), \quad z = u \cdot \sigma(x) + \mu(x), \quad u \sim \mathcal{N}_\epsilon(0, I)$$

Selecting a radius To select a radius, we take the following conservative estimate calculated on a held-out validation set, which computes the smallest ℓ_2 ball under the prior which contains all the mean encodings under the posterior:

$$\epsilon = \max_i \left\| \frac{\mu(x_i, \tilde{x}_i) - \mu(x_i)}{\sigma(x_i)} \right\|_2$$

The benefits of such a selection is that by taking the maximum, we are selecting a learned perturbation set that includes every point with approximation error as low as the posterior encoder. To some extent, this will also capture additional types of perturbations beyond the perturbed data, which can be both beneficial and unwanted depending on what is captured. However, in the context of adversarial attacks, using a perturbation set which is too large is generally more desirable than one which is too small, in order to not underspecify the threat model.

Evaluation metrics We present each evaluation metric in detail for a single perturbed pair (x, \tilde{x}) . These evaluation metrics can then be averaged over the test dataset to produce the evaluations presented in this paper.

1. **Encoder approximation error (Enc. AE)** We can get a fast upper bound of approximation error by taking the posterior mean, unparameterizing it with respect to the prior, and

projecting it to the ϵ ball as follows:

$$\begin{aligned} \text{Enc. AE}(x, \tilde{x}) &\equiv \|\tilde{x} - g(z, x)\|^2 \\ \text{where } z &= u \cdot \sigma(x) + \mu(x), \\ u &= \text{Proj}_\epsilon \left(\frac{\mu(x, \tilde{x}) - \mu(x)}{\sigma(x)} \right) \end{aligned}$$

2. **PGD approximation error (PGD AE)** We can refine the upper bound by solving the following problem with projected gradient descent:

$$\begin{aligned} \text{PGD AE}(x, \tilde{x}) &\equiv \min_{\|u\| \leq \epsilon} \|\tilde{x} - g(z, x)\|^2 \\ \text{where } z &= u \cdot \sigma(x) + \mu(x) \end{aligned}$$

In practice, we implement this by warm starting the procedure with the solution from the encoder approximation error, and run 50 iterations of PGD at step size $\epsilon/20$.

3. **Expected approximation error (EAE)** We can compute this by drawing N samples $u_i \sim \mathcal{N}_\epsilon(0, I, \epsilon)$ and calculating the following Monte Carlo estimate:

$$\begin{aligned} \text{EAE}(x, \tilde{x}) &\equiv \frac{1}{N} \sum_{i=1}^N \|\tilde{x} - g(z_i, x)\|^2 \\ \text{where } z_i &= u_i \cdot \sigma(x) + \mu(x) \end{aligned}$$

In practice, we find that $N = 5$ is sufficient for reporting means over the dataset with near-zero standard deviation.

4. **Over approximation error (OAE)** We can compute this by performing a typical ℓ_2 PGD adversarial attack:

$$\begin{aligned} \text{OAE}(x, \tilde{x}) &\equiv \max_{\|u\| \leq \epsilon} \|\tilde{x} - g(z, x)\|^2 \\ \text{where } z &= u \cdot \sigma(x) + \mu(x) \end{aligned}$$

In practice, we implement this by doing a random initialization and run 50 iterations of PGD at step size $\epsilon/20$.

5. **Reconstruction error (Recon. err)** This is the typical reconstruction error of a variational autoencoder, which is a Monte Carlo estimate over the full posterior with one sample:

$$\begin{aligned} \text{Recon. err}(x, \tilde{x}) &\equiv \frac{1}{m} \|\tilde{x} - g(z, x)\|^2 \\ \text{where } z &= u \cdot \sigma(x, \tilde{x}) + \mu(x, \tilde{x}) \\ u &\sim \mathcal{N}(0, I) \end{aligned}$$

Note that we report the average over all pixels to be consistent with the other metrics in this paper, however it is typical to implement this during training as a sum of squared error instead of a mean.

6. **KL divergence (KL)** This is the standard KL divergence between the posterior and the prior distributions

$$KL(x, \tilde{x}) \equiv KL(\mathcal{N}(\mu(x, \tilde{x}), \sigma(x, \tilde{x})) \| \mathcal{N}(\mu(x), \sigma(x)))$$

C MNIST

In this section, we provide a complete description and discussion of our results on MNIST, consisting of 60,000 training examples with 1,000 examples randomly set aside for validation purposes, and 10,000 examples in the test set. These experiments were run on a single GeForce RTX 2080 Ti graphics card, with the longest perturbation set taking 1 hour to train.

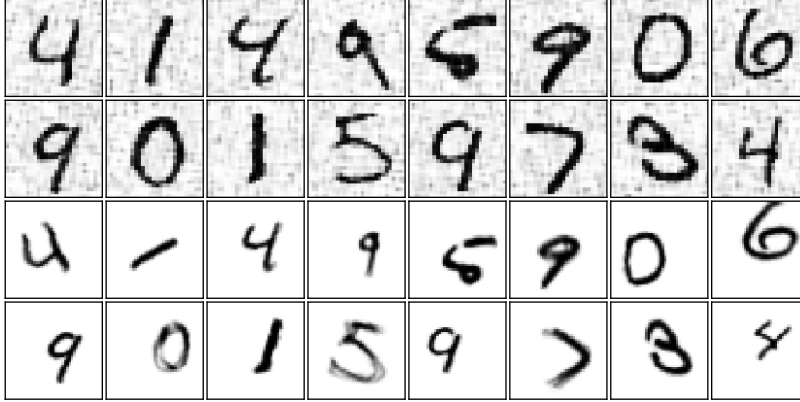


Figure 4: Samples of ℓ_∞ (top) and RTS (bottom) perturbations for MNIST from the convolutional ℓ_∞ and RTS-1 models.

C.1 Experimental details

ℓ_∞ details For the ℓ_∞ setting, perturbations with radius $\epsilon = 0.3$. Our fully connected network encoders have one hidden layer with 784 hidden units, then two linear modules with 784 outputs each for computing the mean and log variance of the latent space distributions. The generator network has the same structure, one hidden layer with 784 hidden units. The posterior and generator networks simply concatenate their inputs into a single vector.

The encoders for the convolutional network for the ℓ_∞ setting uses two hidden convolutional layers with 32 and 64 channels, each followed by ReLU and max pooling. To generate the mean and log variance, there are two final convolution with 128 channels. The posterior network concatenates its inputs via the channel dimension. The generator has two analogous hidden layers using convolutions with 64 and 32 channels followed by ReLU and nearest neighbor upsampling. One final convolution reduces the number of channels to 1, and the conditioned input x is downsampled with 1×1 convolutions and concatenated with the feature map before each convolution. All convolutions other than the downsampling convolutions use a 3×3 kernel with one padding.

Both networks are trained for 20 epochs, with step size following a piece-wise linear schedule of $[0, 0.001, 0.0005, 0.0001]$ over epochs $[0, 10, 15, 20]$ with the Adam optimizer using batch size 128. The KL divergence is weighted by β which follows a piece-wise linear schedule from $[0, 0.001, 0.01]$ over epochs $[0, 5, 20]$.

RTS details For the RTS setting, we follow the formulation studied by Jaderberg et al. [2015], which consists of a random rotation between $[-45, 45]$ degrees, random scaling factor between $[0.7, 1.3]$, and random placement in a 42×42 image. The architecture uses a typical pre-activation convolution block, which consists of 2 convolutions with reflection padding which are pre-activated with batchnorm and ReLU. The encoders uses a single block followed by two linear modules to 128 units to generate the mean and log variance, where the posterior network concatenates its inputs via the channel dimension. The generator has a linear layer to map the latent vector back to a 42×42 feature map, followed by five parallel spatial transformers which use the latent vector to transform the conditioned input. Multiple spatial transformers here are used simply because training just one can be inconsistent. The outputs of the spatial transformers are concatenated via the channel dimension, followed by a convolutional block and one final convolution to reduce it back to one channel.

All networks are trained for 100 epochs with cyclic learning rate peaking at 0.0008 on the 40th epoch with the Adam optimizer using batch size 128. The KL divergence is weighted by β which follows a piece-wise linear schedule from $[0, 0.01, 1, 1]$ over epochs $[0, 10, 50, 100]$.

C.2 Samples and visualizations

Figure 4 plots samples from the convolutional model producing ℓ_∞ perturbations and the RTS model trained with only one perturbed datapoint per example. We note that the final β value for the ℓ_∞

Table 2: Evaluation of a perturbation set learned from MNIST examples perturbed by ℓ_∞ noise with $\epsilon = 0.3$ and RTS perturbations. The standard deviation is less than 0.01 for all metrics except KL divergence.

Model	ϵ	Test set quality metrics				Test set CVAE metrics	
		Enc. AE	PGD AE	EAE	OAE	Recon. err	KL
Fully connected ℓ_∞	28	0.31	0.25	0.32	0.65	0.27	585.5 ± 0.29
Convolutional ℓ_∞	29	0.30	0.27	0.32	0.35	0.27	610.3 ± 0.10
RTS	14	0.29	0.11	0.54	1.03	0.04	22.2 ± 0.02
RTS-1	14	0.28	0.10	0.61	1.34	0.05	22.2 ± 0.03
RTS-5	14	0.28	0.10	0.53	0.86	0.05	23.7 ± 0.02

perturbation was tuned to produce reasonable samples in order to balance the KL divergence and reconstruction error, likely due to the inherent difficulty of this setting.

C.3 Evaluating the perturbation set

Table 2 contains the full tabulated results evaluating the MNIST perturbation sets. The KL divergence for the ℓ_∞ perturbation sets are much higher due to the KL divergence being weighted by 0.01 in order to produce reasonable samples. We note that the convolutional network and fully connected network evaluate to about the same, except that the convolutional network has a much lower overapproximation error and is likely restraining the size of the learned perturbation set.

The RTS-1 results demonstrate how fixing the number of perturbations seen during training to one per datapoint is still enough to learn a perturbation set with as much approximation error as a perturbation set with an infinite number of samples, denoted RTS. Increasing the number of perturbations to five per datapoint allows the remaining metrics to match the RTS model, and so not many samples are needed to learn a perturbation set in this setting.

D CIFAR10 common corruptions

In this section, we describe the CIFAR10 common corruptions setting and experiments in greater detail. The dataset comes with 15 common corruptions covering noise, blurs, weather, and digital corruptions. We omit the three noise corruptions due to similarity to unstructured ℓ_p noise, leaving us with the following 12 corruptions for each example:

1. Blurs: defocus blur, glass blur, motion blur, zoom blur
2. Weather: snow, frost, fog
3. Digital: brightness, contrast, elastic, pixelate, jpeg

The dataset comes with different corruption levels, so we focus on the highest severity, corruption level five, so the total training set has 600,000 perturbations (12 for each of 50,000 examples) and the test set has 120,000 perturbations. The dataset also comes with several additional corruptions meant to be used as a validation set, however for our purposes will serve as a way to measure performance on out-of-distribution corruptions. These are Gaussian blur, spatter, and saturate which correspond to the blur, weather, and digital categories respectively. We generate a validation set from the training set by randomly setting aside 1/50 of the CIFAR10 training set and all of their corresponding corrupted variants. These experiments were run on a single GeForce RTX 2080 Ti graphics card, taking 22 hours to train the CVAE and 28 hours to run adversarial training.

D.1 Perturbation model architecture and training specifics

We use standard preactivation residual blocks [He et al., 2016], with a convolutional bottleneck which reduces the number of channels rather than downsampling the feature space. This aids in learning to produce CIFAR10 common corruptions since the corruptions are reflective of local rather than global changes, and so there is not so much benefit from compressing the perturbation information into a smaller feature map. Specifically, our residual blocks uses convolutions that go from $64 \rightarrow 16 \rightarrow 64$

Table 3: Prior and encoder architecture for learning CIFAR10 common corruptions

Input($3 \times 32 \times 32$)	Input($k \times 32 \times 32$)
Concat($3, k$)	
Conv(64)	
$4 \times$ Residual(64)	
Conv(16)	
FC(512)	FC(512)

Table 4: Decoder architecture for learning CIFAR10 common corruptions

Input(500)	
FC($1 \times 32 \times 32$)	Input($3 \times 32 \times 32$)
Concat(1, 3)	
Conv(64)	
$4 \times$ Residual(64)	
Conv(3)	

Table 5: Measuring and comparing quality metrics for a CVAE perturbation set trained on CIFAR10 common corruptions with different pairing strategies depending on the available information.

Method	ϵ	Test set quality metrics				Test set CVAE metrics	
		Enc. AE	PGD AE	EAE	OAE	Recon. err	KL
Centered at original	28	0.005	0.006	0.029	0.17	$5.73 \cdot 10^{-4}$	69.31
Original + perturbed	34	0.019	0.010	0.035	0.20	$8.33 \cdot 10^{-4}$	160.60
Perturbed only	28	0.019	0.007	0.038	0.17	$8.53 \cdot 10^{-4}$	182.85

channels denoted as Residual(64). Then, our encoder and prior networks are as shown in Table 3, where $k = 0$ for the prior network and $k = 3$ for the encoder network, and the decoder network is as shown in Table 4.

Stabilizing the exponential function Note that the CVAE encoders output the log variance of the prior and posterior distributions, which need to be exponentiated in order to calculate the KL distance. This runs the risk of numerical overflow and exploding gradients, which can suddenly cause normal training to fail. To stabilize the training procedure, it is sufficient to use a scaled Tanh activation function before predicting the log variance, which is a Tanh activation which has been scaled to output a log variance between $[\ln(10^{-3}), \ln(10)]$. This has the effect of preventing the variance from being outside the range of $[10^{-3}, 10]$, and stops overflow from happening. In practice, the prior and posterior converge to a variance within this range, and so this doesn’t seem to adversely effect the resulting representative power of the CVAE while stabilizing the exponential calculation.

Training is done for 1000 epochs using a cyclic learning rate [Smith, 2017], peaking at 0.001 on the 400th epoch using the Adam optimizer [Kingma and Ba, 2014] with momentum 0.9 and batch size 128. The hyperparameter β is also scheduled to increase linearly from 0 to 10^{-2} over the first 400 epochs. We use standard CIFAR10 data augmentation with random cropping and flipping.

D.2 Pairing strategies

Here, we quantitatively evaluate the effect of the different pairing strategies for the CIFAR10 common corruptions setting when training a perturbation set with a CVAE in Table 5. We first note that the approach using random pairs of both original and perturbed data has a larger radius than the others, likely since the generator needs to produce not just the perturbed data but also the original as well. We next see that all metrics across the board are substantially lower for the approach which centers the prior by always conditioning on the unperturbed example, and so if such an unperturbed example is known, we recommend conditioning on said example to learn a better perturbation set.

D.3 Properties of the CVAE latent space

We next study closely the properties of the underlying latent space which has been trained to generate CIFAR10 common corruptions. We summarize a number of statistics in Table 6, namely the mean, standard deviation, and some percentile thresholds where we can clearly see that the latent vectors for the CVAE centered around the original are much smaller in ℓ_2 norm and thus learns the most compact perturbation set. We remind the reader that maximum ℓ_2 norm reported here is calculated on

Table 6: CIFAR10 common corruptions validation set statistics for the ℓ_2 norm of the latent space encodings.

Method	β	Mean	Std	25%	50%	75%	Max
Centered at original	0.01	6.53	5.22	2.69	3.85	10.16	26.61
Original + perturbed	0.01	11.50	4.52	7.81	10.95	14.48	31.30
Perturbed only	0.01	11.04	3.81	7.93	10.82	13.46	29.57

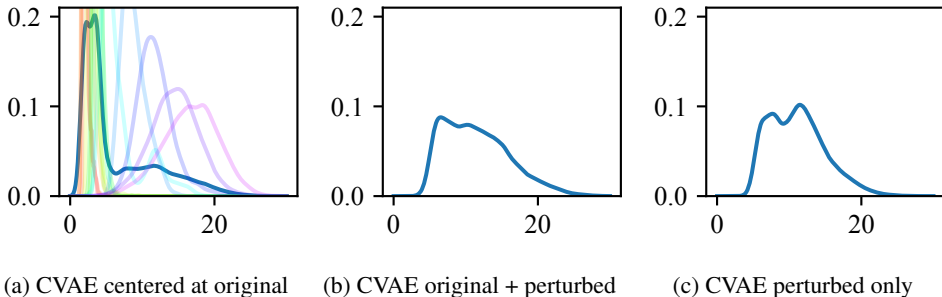


Figure 5: Distribution of ℓ_2 norms for latent encodings of CIFAR10 common corruptions on the test set for each pairing strategy.

the test set and is not necessarily the same as the radius reported in Table 5 since the radius is selected based on a validation set.

Distribution of ℓ_2 distances in latent space We plot the distribution of the ℓ_2 norm of the latent space encodings in Figure 5, and further find the centered CVAE has semantic latent structure. Specifically, corruptions can be ordered by their ℓ_2 norm in the latent space where each corruption inhabits a particular range of distance, so reducing the radius directly constrains the type of corruptions in the perturbation set. For example, restricting the perturbation set to radius $\epsilon = 5$ corresponds to leaving out frost fog, snow, elastic, and glass blur corruptions, while containing all defocus blur, jpeg compression, and motion blur corruptions. A larger version of Figure 5a with a complete legend listing all the corruptions is in Figure 6.

Additional samples and interpolations from the CVAE To further illustrate what corruptions are represented in the CVAE latent space, we plot additional samples and interpolations from the CVAE. In Figure 7 we draw four random samples for eight different examples, which show a range of corruptions and provide qualitative evidence that the perturbation set generates reasonable samples. In Figure 8 we see a number of examples being interpolated between weather, blur, and digital corruptions, which also demonstrate how the perturbation set not only includes the corrupted datapoints, but also variations and interpolations in between corruptions.

D.4 Adversarial training

For learning a robust CIFAR10 classifier, we use a standard wide residual network [Zagoruyko and Komodakis, 2016] with depth 28 and width factor 10. All models are trained with the Adam optimizer with momentum 0.9 for 100 epochs with batch size 128 and cyclic learning rate schedule which peaks at 0.2 at epoch 40. This cyclic learning rate was tuned to optimize the validation performance for the data augmentation baseline, and kept fixed as-is for all other approaches. We use validation-based early stopping for all approaches to combat robust overfitting [Rice et al., 2020]. However, we find that in this setting and also likely due to the cyclic learning rate, we do not observe much overfitting. Consequently, the final model at the end of training ends up being selected for all methods regardless. Adversarial training is done with a PGD adversary at the full radius of $\epsilon = 28$ with step size $\epsilon/5 = 5.6$ and 7 iterations. At evaluation time, for a given radius ϵ we use a PGD adversary with 50 steps of size $\epsilon/20$. Additional examples of adversarial attacks under this adversary are in Figure 9, which still appear to be reasonable corruptions despite being adversarial.

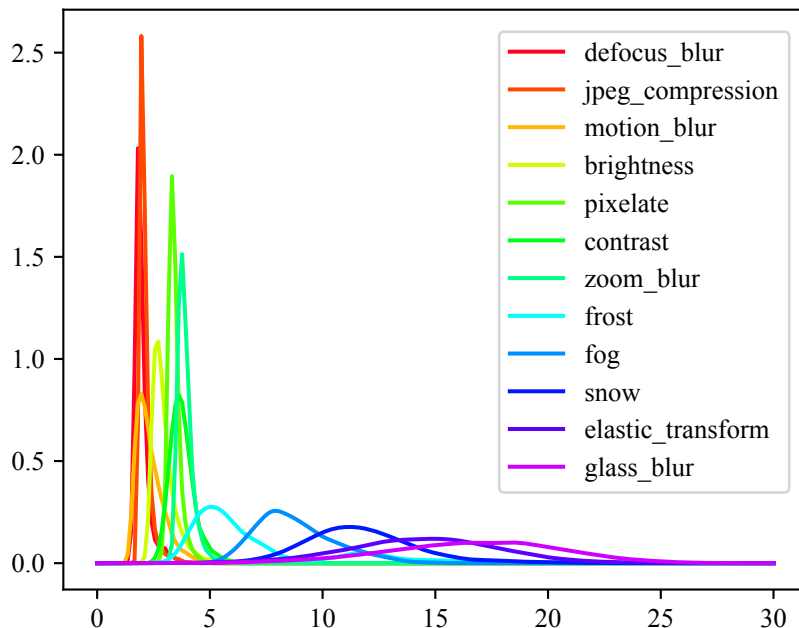


Figure 6: A larger version of the density of the ℓ_2 norms of latent encodings of CIFAR10 common corruptions, broken down by type of corruption.

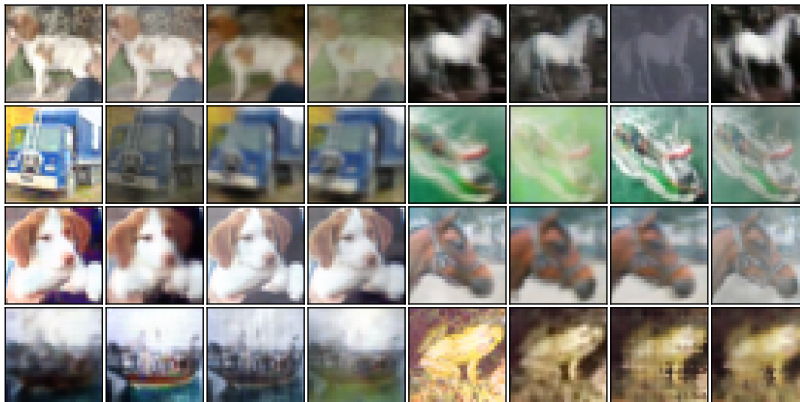


Figure 7: Random perturbations from the CVAE prior, showing four random samples for each example.

D.5 Randomized smoothing

Randomized smoothing is done in its most basic form, with normal Gaussian data augmentation at the specified noise level σ . We predict labels with $n_0 = 100$ samples and do certification with $n = 10,000$ samples at confidence $\alpha = 0.001$, so each example has a 0.1% chance of being incorrectly certified. Unlike in the typical setting, we have a known maximum radius for the perturbation set. This allows us to backwards engineer a noise level to have a specific maximum certified radius as follows: let ℓ be the maximum possible lower bound obtained from a confidence interval at level $1 - \alpha$ with n classifications that are in unanimous agreement. Then, the maximum certifiable radius is $r = \sigma \Phi^{-1}(\ell)$ where Φ^{-1} is the inverse cumulative distribution function of a standard normal distribution. By setting $r = \epsilon$, we can solve for the desired noise level $\sigma = \frac{\epsilon}{\Phi^{-1}(\ell)}$ to naturally select a noise level with maximum certified radius ϵ . We do this for the $\epsilon \in \{2.7, 3.9, 10.2\}$

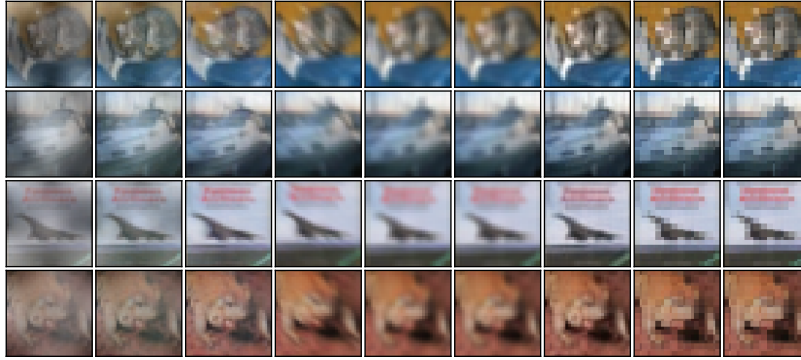


Figure 8: Interpolations between fog (left), defocus blur (middle), and pixelate (right) corruptions as representative distinct types of corruptions from the weather, blur, and digital corruption categories.

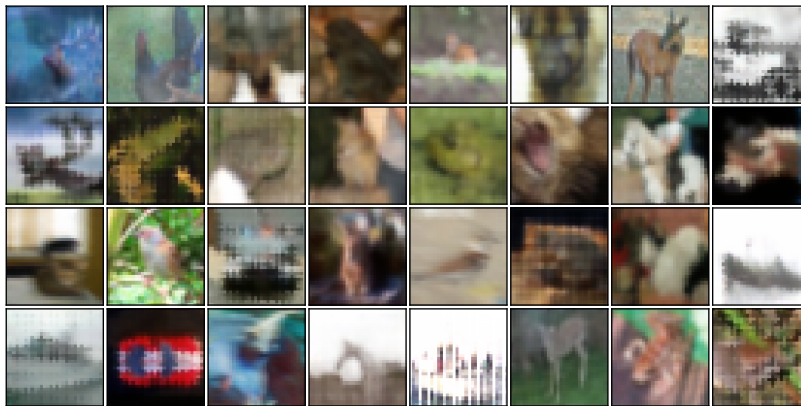


Figure 9: Adversarial examples that cause misclassification for an adversarially trained classifier.

which are the 25th, 50th, and 75th percentiles of the perturbation set, and get $\sigma \in \{0.84, 1.22, 3.19\}$ respectively.

The results of randomized smoothing at these thresholds are presented in Table 7. Note that by construction, each noise level cannot certify a radius larger than what is calculated for. We find that clean accuracy isn't significantly harmed when smoothing at the lower noise levels, and actually improves perturbed accuracy over the adversarial training approach from Table 1 but with lower out-of-distribution accuracy than adversarial training. However, all noise levels are able to achieve non-trivial degrees of certified robustness, with the highest noise level being the most robust but also taking a hit to standard test set accuracy metrics. Most notably, due to the latent structure present in the perturbation set as discussed in Appendix D.3, even the ability to certify small radii translates to meaningful provable guarantees against certain types of corruptions, like defocus blur and jpeg compression which are largely captured at radius $\epsilon = 3.9$.

We note that although the largest noise level can theoretically reach the 75th percentile of the perturbation set at radius $\epsilon = 10.2$, none of the examples can be certified to that extent. This is possibly a limitation of the certification procedure, since although a noise level of $\sigma = 3.19$ can theoretically certify a radius of up to $\epsilon = 10.2$, the ℓ_2 norm of the random samples needed to perform randomized smoothing is approximately 23, which is well beyond the 75th percentile and towards the boundary of the perturbation set. The complete robustness curves for all three noise levels are plotted in Figure 10.

Table 7: Certified robustness to CIFAR10 common corruptions with a CVAE perturbation set.

Noise level	Test set accuracy (%)			Test set certified accuracy (%)		
	Clean	Perturbed	OOD	$\epsilon = 2.7$	$\epsilon = 3.9$	$\epsilon = 10.2$
$\sigma = 0.84$	93.8	92.5	84.2	34.7	00.0	00.0
$\sigma = 1.22$	94.0	92.6	83.9	66.1	15.3	00.0
$\sigma = 3.19$	86.7	84.7	65.0	86.7	39.4	00.0

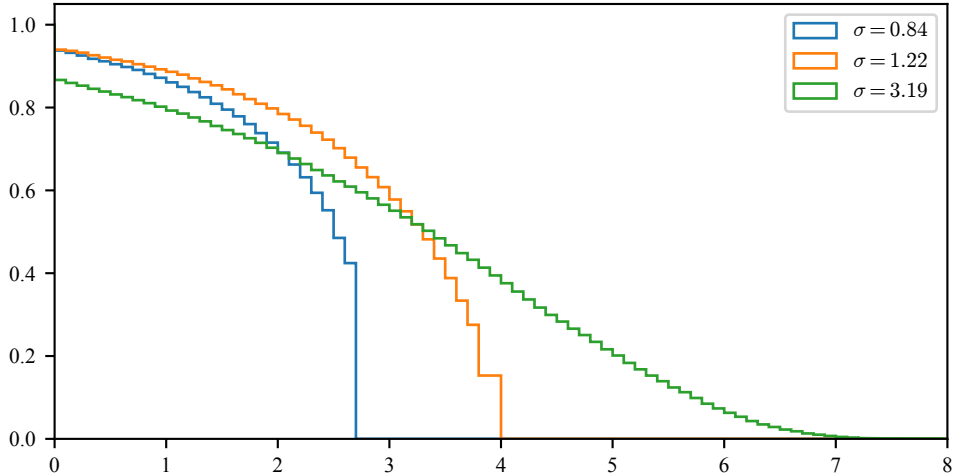


Figure 10: Certified accuracy against CIFAR10 common corruptions using randomized smoothing at various noise levels. The horizontal axis plots the certified radius, and the vertical axis plots the fraction of examples certified at that radius.

E Multi-illumination

In this final section we present the multi-illumination experiments in greater detail with an expanded discussion. We use the test set provided by Murmann et al. [2019] which consists of 30 held out scenes and hold out 25 additional “drylab” scenes for validation. Unlike in the CIFAR10 common corruptions setting, there is no such thing as an “unperturbed” example in this dataset so we train on random pairs selected from the 25 different lighting variations for each scene. These experiments were run on a single Quadro RTX 8000 graphics card, taking 16 hours to train the CVAE and 12 hours to run adversarial training.

E.1 Architecture and training specifics

We convert a generic UNet architecture [Ronneberger et al., 2015] to use as a CVAE, by inserting the variational latent space in between the skip connections of similar resolutions. At a high level, the encoder and prior networks will be based on the downsampling half of a UNet architecture, the conditional generator will be based on the full UNet architecture, and the components will be linked via the latent space of the VAE. Specifically, our networks have [64, 128, 256, 512, 512] channels when downsampling, and twice the number of channels when upsampling due to the concatenation from the skip connection. Each skip connection passes through a 1×1 convolution that reduces the number of channels to 16, and an adaptive average pooling layer that reduces the feature maps to height and width [(127, 187), (62, 93), (31, 46), (15, 23), (7, 11)] respectively. The adaptive average pooling layer has the effect of a null operator for the MIP5 resolution, but allows higher resolutions to use the same architecture. These fixed-size feature maps are then passed through a fully connected layer to output a mean and log variance for the latent space with dimension [128, 64, 32, 16, 16] for each respective feature map. The concatenation of all the latent vectors from each skip connection forms the full, 256 dimensional latent space vector for the CVAE. Similar to the CIFAR10 setting, we use a scaled Tanh activation to stabilize the log variance calculation.

Table 8: Measuring and comparing quality metrics for a multi-illumination CVAE at different resolutions.

Resolution	ϵ	Test set quality metrics				Test set CVAE metrics	
		Encoder AE	PGD AE	OAE	EAE	Recon. err	KL
MIP5 (125 × 187)	17	0.019	0.006	0.049	0.13	0.0040	65.8
MIP4 (250 × 375)	25	0.034	0.008	0.049	0.27	0.0042	146.6
MIP3 (500 × 750)	21	0.060	0.009	0.048	0.33	0.0055	106.1

Table 9: Multi-illumination validation set statistics for the ℓ_2 norm of the latent space encodings.

Resolution	β	Mean	Std	25%	50%	75%	Max
MIP5 (125 × 187)	1	7.42	2.14	5.93	7.35	8.81	16.63
MIP4 (250 × 375)	1	10.88	3.18	8.69	10.75	12.95	24.69
MIP3 (500 × 750)	10	9.11	2.72	7.14	9.00	10.97	20.65

The generator of the CVAE UNet is implemented as a typical UNet that takes as input the conditioned example, where intermediate feature maps are concatenated with extra feature maps from the latent space of the CVAE. Specifically, each latent space sub-vector is mapped with a fully connected layer back to a feature map with size $[(127, 187), (62, 93), (31, 46), (15, 23), (7, 11)]$ with one channel. It is then interpolated to the actual feature map size of the UNet (which is a no-op for the MIP5 resolution) and concatenated to the standard UNet feature map before upsampling.

We train the model for 1000 epochs with batch size 64, using the Adam optimizer with 0.9 momentum, weight decay $5 \cdot 10^{-7}$, and a cyclic learning rate from $[0.0001, 0.001, 0]$ over $[0, 400, 1000]$ epochs. Same as in the CIFAR10 setting, the learning rate and weight decay were chosen to optimize the validation performance of the baseline data augmentation approach and kept fixed as-is for all other methods. We weight the KL divergence with a β hyperparameter which is scheduled from $[0, 1, 1]$ over $[0, 400, 1000]$, using random flip and crop with padding of 10 for data augmentation. We then fine tune the model for higher resolutions: for MIP4 we fine tune for 100 epochs with the same learning rate schedule scaled down by a factor of 4, and for MIP3 we fine tune for 25 epochs with the learning rate schedule scaled down by 40. In order to keep the samples looking reasonable, for MIP3 we also increase the β weight on the KL divergence to 10. Random cropping augmentation is proportionately increased with the size of the image, using padding of 20 and 40 for MIP4 and MIP3 respectively.

Learning and evaluating an illumination perturbation set at multiple scales The results of this fine tuning procedure to learn a perturbation at higher resolutions are summarized in Tables 8 and 9. As expected, the quality metrics of the perturbation set get slightly worse at higher resolutions which is counteracted to some degree by the increase in weighting for the KL divergence at MIP3. Despite using the same architecture size, the perturbation set is able to reasonably scale to images with 16 times more pixels and generate reasonable samples while keeping relatively similar quality metrics. However, to keep computation requirements at a reasonable threshold, we focus our experiments at the MIP5 resolution, which is sufficient for our robustness tasks.

E.2 Additional samples and interpolations from the CVAE

We present additional samples and interpolations of lighting changes learned by the CVAE perturbation set. Figure 11 shows interpolations between three randomly chosen lighting perturbations for four different scenes, while Figure 12 shows 24 additional random samples from the perturbation set, showing a variety of lighting conditions. These demonstrate qualitatively that the perturbation set contains a reasonable set of lighting changes.

E.3 Adversarial training and randomized smoothing

In this final task, we leverage our learned perturbation set to learn a model which is robust to lighting perturbations. Specifically the multi-illumination dataset comes with annotated material

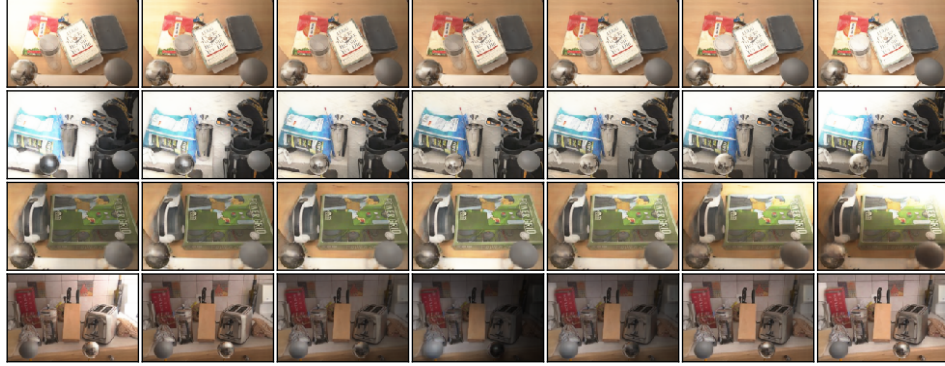


Figure 11: Additional interpolations between three (left, middle, right) randomly chosen lighting perturbations in each row.



Figure 12: Additional random samples from the CVAE prior showing variety in lighting perturbations in various different scenes.

maps that label each pixel with the type of material (e.g. fabric, plastic, and paper), so a natural task to perform in this setting is to learn material segmentation maps. We report robustness results at $\epsilon \in \{7.35, 8.81, 17\}$ which correspond to the 50th, 75th, and 100th percentiles. We select a fixed lighting angle which appears to be neutral and train a material segmentation model to generate a baseline, which achieves 37.2% accuracy on the test set but only 14.9% robust accuracy under the full perturbation model.

We evaluate several methods for improving robustness of the segmentation maps to lighting perturbations, namely data augmentation with the perturbed data, data augmentation with the CVAE, and adversarial training with the CVAE. The results are tabulated in Table 10. The CVAE data augmentation approach is not as effective in this setting at improving robust accuracy, as the pure data augmentation approach does reasonably well. However, the adversarial training approach unsurprisingly has the most robust accuracy, maintaining 35.4% robust accuracy under the full perturbation set at $\epsilon = 17$ and outperforming the data augmentation approaches. We plot adversarial perturbations at $\epsilon = 7.35$ and the resulting changed segmentation maps in Figure 13 for a model trained with pure data augmentation and in Figure 14 for a model trained to be adversarially robust, the latter of which has, on average, less pixels that are effected by an adversarial lighting perturbation. Adversarial examples at the full radius of $\epsilon = 17$ are shown in Figure 15, where we see that the perturbation set is beginning to cast dark shadows over regions of the image to force the model to fail.

Finally, we train a certifiably robust material segmentation model using the perturbation set. We train using a noise level of $\sigma = 6.90$ which can certify a radius of at most $\epsilon = 17$, or the limit of the perturbation set. The resulting robustness curve is plotted in Figure 16. The model achieves 30.7% perturbed accuracy and is able to get 12.4% certified accuracy at the 50th percentile of radius $\epsilon = 7.35$. The key takeaway is that we can now certify real-world perturbations to some degree, in this case certifying robustness to 50% of lighting perturbations with non-trivial guarantees.

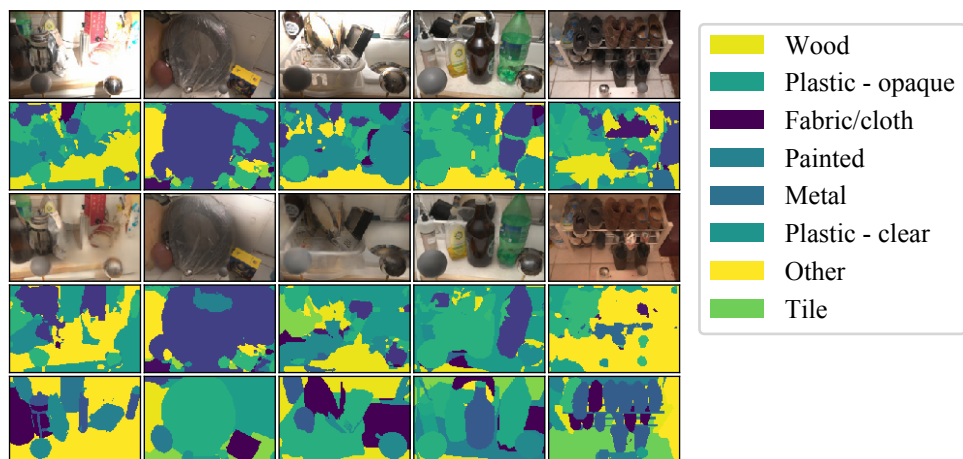


Figure 13: Adversarial examples that can cause on average 9.9% more pixels in the shown segmentation maps to be incorrect for a model trained with data augmentation. The first two rows are a benign lighting perturbation and its corresponding predicted material segmentation, and the next two rows are an adversarial lighting perturbation and its corresponding predicted material segmentation. For reference, the final row contains the true material segmentation.

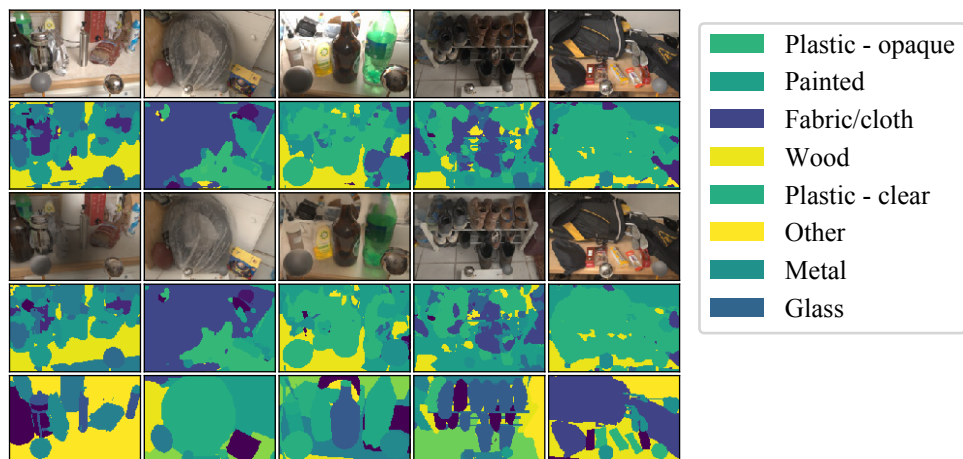


Figure 14: Adversarial examples that can cause on average 3% more pixels in the shown segmentation maps to be incorrect for an adversarially trained model.

Table 10: Learning image segmentation models that are robust to changes in lighting with a CVAE perturbation set.

Method	Test set accuracy (%)		Test set robust accuracy (%)		
	Perturbed	$\epsilon = 7.35$	$\epsilon = 8.81$	$\epsilon = 17$	
Fixed lighting angle	37.2	26.3	24.2	14.9	
Data augmentation	45.2	38.0	36.5	27.1	
CVAE data augmentation	41.5	35.5	33.9	24.7	
CVAE adversarial training	41.7	39.4	38.8	35.4	

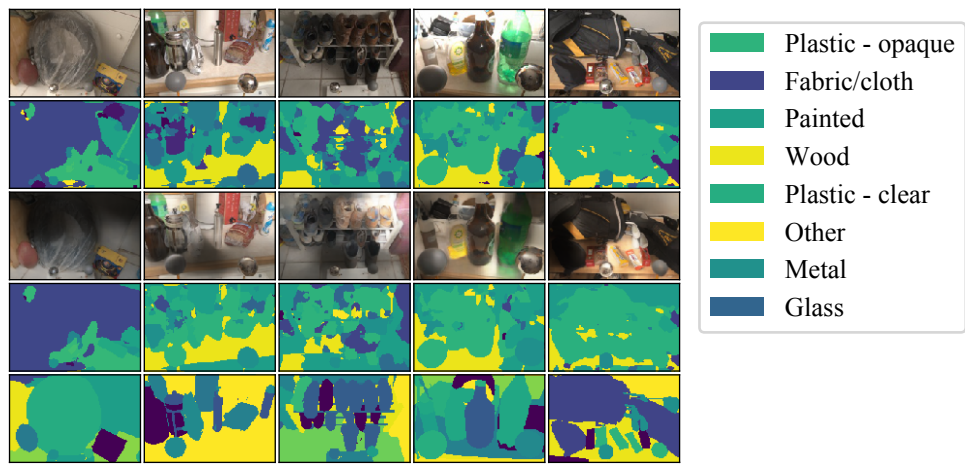


Figure 15: Adversarial examples at the full radius of $\epsilon = 17$ that for an adversarially trained model, which are starting to cast dark shadows to obscure the objects in the image.

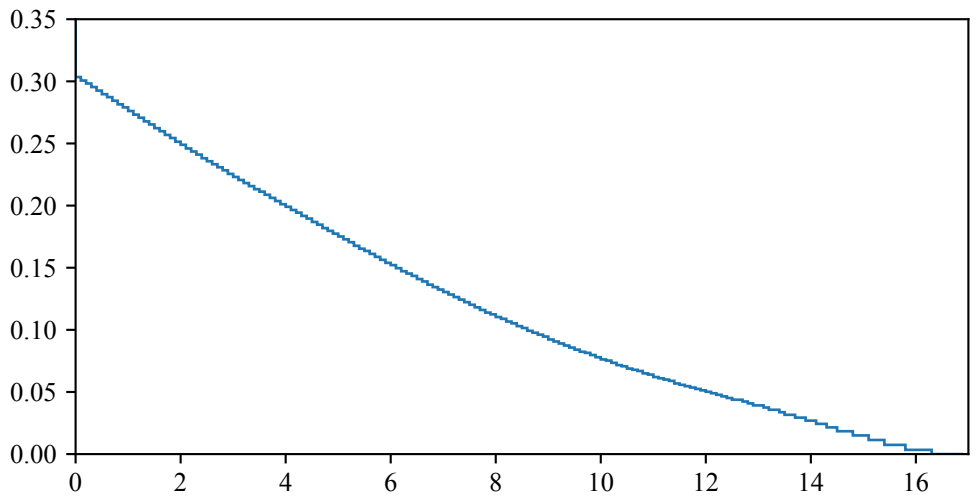


Figure 16: Certified accuracy for material segmentation model using randomized smoothing. The horizontal axis denotes the certified radius, and the vertical axis denotes the fraction of pixels that are certifiably correct at that radius. Note that a radius of $\epsilon = 17$ is the maximum radius of the perturbation set.